Delta-Gap Port Model for Surface-Volume-Surface Electric Field Integral Equation

by

Ammar Aljamal

A Thesis Submitted to the Faculty of Graduate Studies of

The University of Manitoba

in partial fulfillment of the requirements of the degree of

Master of Science

Department of Electrical and Computer Engineering

University of Manitoba

Winnipeg, Manitoba, Canada

Abstract

This thesis presents a δ-gap source model for recently introduced Surface-Volume-Surface Electric Field Integral Equation (SVS-EFIE). The SVS-EFIE is a class of single-source integral equations (SSIEs), which is obtained from the combination of the volumetric equivalence principle with the conventional single-source field representation. The classical δ-gap port model is extended for use in SVS-EFIE for solution of antenna radiation problem, extraction of network parameters in 3D interconnects, and characterization of the microwave circuits. The δ-gap source model for SVS-EFIE is derived from the conventional δ-gap model used in the classical surface EFIE. However, due to single-source nature of the SVS-EFIE equation the net current in the port is determined through integration of the volumetric conductivity current density in the port cross-section. The proposed δ-gap driven SVS-EFIE is discretized using Method of Moments (MoM) with Rao-Wilton-Glisson (RWG) basis functions representing the surface current and piece-wise basis functions in the tetrahedrons discretizing the current in the conductor volume.

The proposed model of port excitation in SVS-EFIE is validated through the studies of the current distribution and the frequency-dependent input impedance of a dipole antenna. Extracted input impedance values obtained with SVS-EFIE are compared against those in the classical EFIE as well as experimental values. Convergence analysis of the computed values of the input impedance with progressively increasing densities of the MoM meshes is performed. Input impedance extracted with

δ-gap excited SVS-EFIE shows stable values upon mesh refinement unlike those in the standard surface EFIE driven by δ-gap port. This mesh stability of the extracted network parameters upon δ-gap excitation as well as the ability of the SVS-EFIE to rigorously compute volumetric field behaviour and, hence, loss behaviour in the presence of skin-, corner- and proximity-effects makes it an attractive alternative to the classical EFIE solutions for antenna analysis and circuit characterization.

Acknowledgments

I would extend my sincerest gratitude to Dr. Vladimir Okhmatovski for all his support and motivation during my master program. This work would not be completed without his guidance and inspiration.

I am grateful to all my friends and colleagues whom I have had the pleasure to work with during my master's program.

I would like to express my gratitude to Natural Sciences and Engineering Research Council of Canada, the University of Manitoba, and the Faculty of Graduate Studies for providing me with sufficient funds and finical support to complete my research work.

To my parents, my siblings and my beloved wife thank you for your support and for being there for me.

To my beloved ...

Contents

List of Figures

List of Tables

Abbreviations

CEM	**C**omputational **E**lectromagnetic
CFIE	**C**ombined **F**ield **I**ntegral **E**quation
CPU	**C**entral **P**rocessing **U**nit
EFIE	**E**lectric **F**ield **I**ntegral **E**quation
EM	**E**lctro**M**agnetic
FDM	**F**inite **D**ifference **M**ethod
FEM	**F**inite **E**lement **M**ethod
MFIE	**M**agnetic **F**ield **I**ntegral **E**quation
MoM	**M**ethod **o**f **M**oments
PEC	**P**erfect **E**lectric **C**onductor
RWG	**R**ao-**W**ilton-**G**lisson basis functions
SD	**S**kin **D**epth
SE	**S**kin **E**ffect
SIE	**S**urface **I**ntegral **E**quation
SSIE	**S**ingle **S**ource **I**ntegral **E**quation
SVS-EFIE	**S**urface-**V**olume-**S**urface **E**lectric **F**ield **I**ntegral **E**quation
SWG	**S**chaubert-**W**ilton-**G**lisson basis functions
V-EFIE	**V**olume- **E**lectric **F**ield **I**ntegral **E**quation
VIE	**V**olume **I**ntegral **E**quation
2-D	**T**wo **D**imensional
3-D	**T**hree **D**imensional

Symbols

$\hat{\mathbf{x}}$, $\hat{\mathbf{y}}$, $\hat{\mathbf{z}}$	Unit vectors in the x, y and z directions.
$\hat{\mathbf{n}}$	normal unit vector outward to the boundary.
$\hat{\mathbf{t}}$	Tangential unit vector to the boundary.
$\mathbf{r}$, $\mathbf{r}$	Position vectors in the Cartesian coordinate system.
ϵ_0	Permittivity of free-space.
ϵ_r	Relative complex permittivity of the scatterer.
σ	Conductivity of the scatterer.
μ_0	Permeability of free-space.
μ_r	Relative permeability of the scatterer.
k_0	Wavenumber of free-space.
k_ϵ	Wavenumber inside the scatterer.
ω	Radial frequency.
f	Frequency of operation.
$\mathtt{t}$	Time variable.
λ	Wavelength.
Γ	Gram matrix.
$\boldsymbol{E}(\mathbf{r}, \mathtt{t})$	Time domain electric-field intensity.
$\boldsymbol{H}(\mathbf{r}, \mathtt{t})$	Time domain magnetic-field intensity.
$\boldsymbol{B}(\mathbf{r}, \mathtt{t})$	Time domain magnetic-field density.
$\boldsymbol{D}(\mathbf{r}, \mathtt{t})$	Time domain electric-field density.
$\boldsymbol{M}(\mathbf{r}, \mathtt{t})$	Time domain impinging magnetic current density.
$\boldsymbol{J}(\mathbf{r}, \mathtt{t})$	Time domain impinging electric current density.

$\mathbf{E}^{\text{inc}}(\mathbf{r})$	Time-harmonic incident electric-field .
$\mathbf{H}^{\text{inc}}(\mathbf{r})$	Time-harmonic incident magnetic-field .
$\mathbf{E}^{\text{scat}}(\mathbf{r})$	Time-harmonic scattered electric-field.
$\mathbf{E}(\mathbf{r})$	Time-harmonic total electric-field.
$\mathbf{H}(\mathbf{r})$	Time-harmonic total magnetic-field.
$\boldsymbol{j}$	Polarization electric current density.
$\boldsymbol{m}$	Polarization magnetic current density.
$\boldsymbol{\mathcal{J}}$	Fictitious surface electric current density.
$\boldsymbol{\mathcal{M}}$	Fictitious surface magnetic current density.
$\overline{\overline{G}}_{e0}$	Dyadic electric Green's function of free space.
$\overline{\overline{G}}_{e\epsilon}$	Dyadic electric Green's function of the scatterer.
∂S	Boundary of the 2D object.
S	Surface of the 2D object.
∂V	Boundary of the 3D object.
V	Volume of the 3D object.
Re	Real part.
Im	Imaginary part.
$\boldsymbol{\nabla}$	Gradient operator.
$\boldsymbol{\nabla}\cdot$	Divergence operator.
$\boldsymbol{\nabla}\times$	Curl operator.
$\boldsymbol{\nabla}\times\boldsymbol{\nabla}\times$	Curl curl operator.
$\langle\cdot\,,\cdot\rangle$	Inner product.

Chapter 1

Introduction

1.1 Motivation

The significance of electromagnetic analysis is growing considerably and becomes essential for an accurate analysis of the current flow in 3D conductors. Current flow modeling in 3D conductors and extraction of the network parameters have important and practical applications in design of RF integrated circuit, high-speed interconnects, power system simulations, and others [1].

The antenna characterization has been a long standing problem in computational electromagnetics [2]. One of the main quantities of interest in the antenna analysis is the input impedance at the feed location. It can be computed by allocating a reasonable feed model at the terminals and considering the antenna as an impedance terminating transmission line (e.g. a coaxial cable) which is used to feed the antenna [3]. The delta-gap source model is the most commonly used excitation model due to its simplicity [4]. It can be used in a wide range of practical antenna models over a wide range of frequencies. The delta-gap model allows the network parameters of multi-port antenna system to be obtained easily as the input-admittance matrix [6]. This model considers an impressed voltage in the gap region of finite width between two wire segments. Such impressed voltage produces the electric field across the gap

between the conductors and forces the current flow in them.

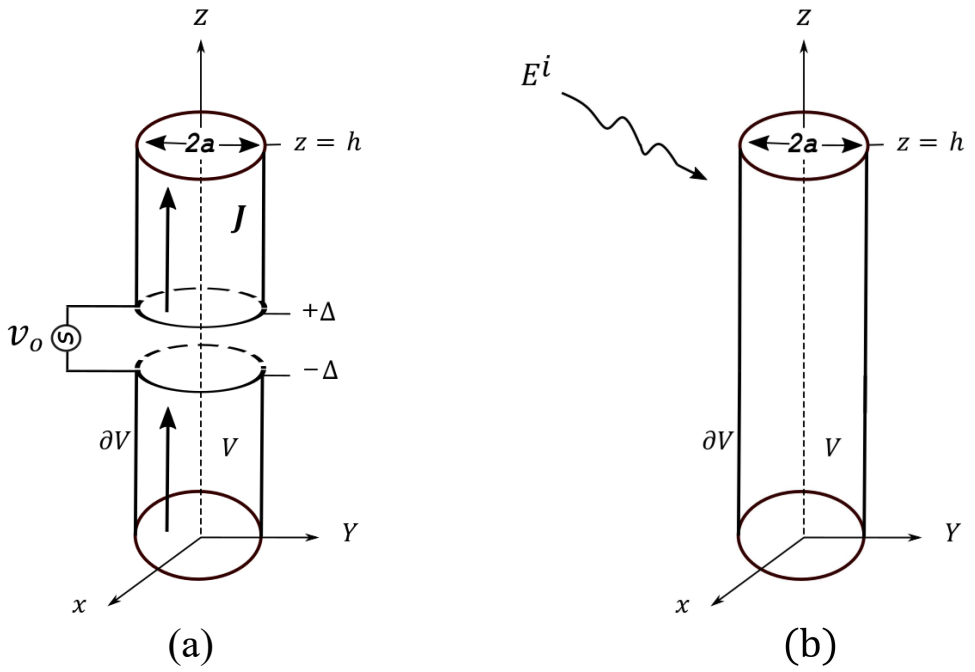

FIGURE 1.1: Two geometries of straight thin wire of length h and radius a with two methods of excitation. The wire acts as a transmitter (a) when it is excited by an impressed voltage across small gap "Delta-Gap Excitation" or acts as a receiver (b) when the wire is excited by an incident plane wave.

The boundary value problems of electromagnetics under given port excitation can be solved directly by using Finite Element Method (FEM) [7] or Finite-Difference-Time-Domain (FDTD) method for discretization of the pertinent partial differential equations [8]. Alternatively, they can be formulated in the equivalent form of integral equations which are solved with Method of Moments (MoM) [9].

Unlike the methods based on direct solution of the partial differential equations, the integral equation formulations require discretization of only the antenna itself and not the space surrounding it.

Various forms of integral equations can be used for analysis of different types of antennas. The classic IE formulations that are used to solve scattering problems on piece-wise homogeneous penetrable objects are the Electric Field Integral Equation (EFIE) [9], the Magnetic Field Integral Equation (MEIE) [9] and the linear combinations between the two fields equations which known as Combined Field Integral Equation (CFIE) [10], [9], the Müller Integral Equation (Müller-IE) [11], the Pogglio-Miller-Chu-Harrington-Wu-Tai Integral Equation (PMCHWT-IE) [12] and others.

The integral equation that is used to solve scattering problems on inhomogeneous penetrable objects is known as the Volumetric Integral Equation (V-IE). It has the advantage of being able to accurately capture the field within the entire frequency range without undergoing the low-frequency breakdown, unlike the classic surface formulations of integral equations. However, solution of the V-IE comes with very high computational and memory costs due to the discretization of the entire volume of the object (e.g. antenna) while producing dense matrix equation.

The conventional surface integral equations possess two unknown functions, the electric and magnetic currents, they also feature kernels with first/second derivatives. In order to diminish the computational complexity associated with the solution of the traditional integral equations the Single Source Integral Equation (SSIE) were introduced [13, 43]. However, having a single unknown results in some drawbacks as the number of kernels increases and the number of integral operators products increases as well, both of which complicate the MoM implementation.

Recently, a new single source integral equation known as Surface-Volume-Surface Integral Equation (SVS-EFIE) [14, 42] was proposed to simplify SSIE formulations. It offers some advantages compared to the traditional SSIE as it has only a single

unknown function on the surface of the scatterer and features fewer integral operators products involved in the formulation. Furthermore, it only has the electrical field Green's functions which allows to shift the derivative operators off the kernels, hence, simplifying its implementation in multi-layered media [15].

1.2 Thesis Research Scope

In this thesis, the SVS-EFIE which is a novel type of SSIE is applied for solution scattering and radiation problems in the presence of imperfect 3-D conductors. The delta-gap model is generalized to enable its use with the SVS-EFIE. The proposed port excitation model enables extraction of the input impedance at the location of the excitation source.

The SVS-EFIE applied to analysis of antennas formed by 3-D imperfect conductors takes advantage of sparsity provided to the discretization matrices due to strong skin-effect per previously done studies [16]. The implementation of the delta-gap source model in the SVS-EFIE formulation is used to solve the problem of dipole antenna radiation and its characterization in terms of the input impedance.

An overview of the fundamental theory in electromagnetics is given in Chapter 2 with a literature review of the primary knowledge required to conduct this research work. The integral equations are formulated through the equivalence principle to lay ground for the derivation of the SVS-EFIE in Chapter 3. It also describes the SVS-EFIE discretization using MoM. In Chapter 4, EFIE and SVS-EFIE formulations are represented with delta-gap source. The discretization of the source model is briefly described in the Chapter 4 as well. Chapter 5 presents numerical SVS-EFIE solution for dipole antenna excited with a delta-gap source. Chapter 6 summarizes results described in the thesis and suggests an outline for future work.

Chapter 2

Maxwell's Equations and Equivalence Principle Formulation

2.1 Maxwell's Equations

In the nineteenth century [17] the physicist James Clerk Maxwell [1831-1879] demonstrated a set of four equations which are the fundamental principles of electromagnetics. Maxwell united two well-known experimental laws: Ampere's Law and Faraday's Law into a coherent and symmetric set of equations that are recognized as Maxwell's Equations.

Maxwell's Equations are the rules that govern the behavior of the magnetic and the electric fields in the universe, where these equations provide a conceptual understanding of how magnetic and electric fields are produced from each other.

When the flow of electric current is varying with time, a magnetic field will be generated. Also, a time-varying magnetic field will give rise to an electric field [18].

The first two equations explain how fields change in space due to sources. Gauss's law for electric field describes how positive or negative charge gives rise to the electric field, whereas Gauss's magnetism law indicates that magnetic charges or monopoles do not exist. The other two equations define the distribution of the field around their

sources. Ampere-Maxwell law explains how magnetic field surrounds time-varying electric field, whereas Faraday's law describes the distribution of electric field around time-varying magnetic field [18].

2.1.1 Maxwell's equations: time domain

Maxwell's equations in time domain can be expressed as following:

$$\boldsymbol{\nabla} \cdot \boldsymbol{D}(\mathbf{r}, \mathtt{t}) = \rho_v(\mathbf{r}, \mathtt{t}), \tag{2.1}$$

$$\boldsymbol{\nabla} \cdot \boldsymbol{B}(\mathbf{r}, \mathtt{t}) = 0, \tag{2.2}$$

$$\boldsymbol{\nabla} \times \boldsymbol{E}(\mathbf{r}, \mathtt{t}) = -\frac{\partial}{\partial \mathtt{t}} \boldsymbol{B}(\mathbf{r}, \mathtt{t}), \tag{2.3}$$

$$\boldsymbol{\nabla} \times \boldsymbol{H}(\mathbf{r}, \mathtt{t}) = \boldsymbol{J}(\mathbf{r}, \mathtt{t}) + \frac{\partial}{\partial \mathtt{t}} \boldsymbol{D}(\mathbf{r}, \mathtt{t}), \tag{2.4}$$

where $\boldsymbol{E}$ is the electric field intensity, $\boldsymbol{D}$ is the electric flux density, $\boldsymbol{H}$ is the magnetic field intensity, $\boldsymbol{B}$ is the magnetic flux density, $\boldsymbol{J}$ is the electric current density, ρ_v is the total electric charge density, $\mathbf{r}$ is a position vector and $\mathtt{t}$ indicates that such quantity is a function of time.

2.1.2 Maxwell's equations: time-harmonic domain

Maxwell's equations are linear differential equations with arbitrary time dependence, therefore, they can be expanded into Fourier transform and characterized in the frequency domain as a function of position $\mathbf{r}$ for frequency f. The time-harmonic Maxwell's equations are:

$$\boldsymbol{\nabla} \cdot \mathbf{D}(\mathbf{r}) = \rho_v(\mathbf{r}), \tag{2.5}$$

$$\boldsymbol{\nabla} \cdot \mathbf{B}(\mathbf{r}) = 0, \tag{2.6}$$

$$\boldsymbol{\nabla} \times \mathbf{E}(\mathbf{r}) = -i\omega \mathbf{B}(\mathbf{r}), \tag{2.7}$$

$$\boldsymbol{\nabla} \times \mathbf{H}(\mathbf{r}) = \mathbf{J}(\mathbf{r}) + i\omega \mathbf{D}(\mathbf{r}), \tag{2.8}$$

where $\mathbf{r}$ is a position vector in space, ω is the angular frequency (radians per second) given by the following expression: $\omega = 2\pi f$ and $i = \sqrt{-1}$ provides an indication about quantity that it is a spectrum and not a function of time $\mathtt{t}$.

2.2 Electromagnetic Wave Equation

The term wave is used to denote a field that is a function of space and time coordinates. A wave equation is a second-order differential equation that describes the propagation of the wave. Electromagnetic field obeys the wave equation which describes the propagation of the electromagnetic wave in a vacuum or through a medium [19].

The electromagnetic wave equation is derived from Maxwell's equations where Ampere's law and Faraday's law can be combined to introduce a wave equation that demonstrates the existence of electromagnetic wave propagation with a velocity equal to the velocity of light.

Let's assume an electromagnetic wave in a source-free region with electric charge density ρ_v and electric current density equal to zero, as in the wave propagation problem the origin of the wave and how it is generated is not of interest.

For isotropic and homogeneous medium that is characterized by permittivity ϵ and permeability μ, Maxwell's equations can be reduced to [18]

$$\boldsymbol{\nabla} \times \boldsymbol{E} = -\mu \frac{\partial}{\partial \mathtt{t}} \boldsymbol{H}, \tag{2.9}$$

$$\boldsymbol{\nabla} \times \boldsymbol{H} = \epsilon \frac{\partial}{\partial \mathtt{t}} \boldsymbol{E}, \tag{2.10}$$

$$\boldsymbol{\nabla} \cdot \boldsymbol{E} = 0, \tag{2.11}$$

$$\boldsymbol{\nabla} \cdot \boldsymbol{H} = 0. \tag{2.12}$$

Equations (2.9-2.12) are first-order differential equations with two variables $\boldsymbol{E}$ and $\boldsymbol{H}$. Combination of these equations yields a second-order differential equation in terms of $\boldsymbol{E}$ or $\boldsymbol{H}$ alone.

Let's take the curl of equation (2.9) and use equation (2.10), that is

$$\boldsymbol{\nabla} \times \boldsymbol{\nabla} \times \boldsymbol{E} = -\mu \frac{\partial}{\partial \mathtt{t}} (\boldsymbol{\nabla} \times \boldsymbol{H}) = -\mu\epsilon \frac{\partial^2}{\partial \mathtt{t}^2} \boldsymbol{E} \tag{2.13}$$

Using the following identity

$$\boldsymbol{\nabla} \times \boldsymbol{\nabla} \times \boldsymbol{E} = \boldsymbol{\nabla}(\boldsymbol{\nabla} \cdot \boldsymbol{E}) - \boldsymbol{\nabla^2} \boldsymbol{E}, \tag{2.14}$$

where $\boldsymbol{\nabla} \cdot \boldsymbol{E} = 0$ in (2.11), yields

$$\boldsymbol{\nabla} \times \boldsymbol{\nabla} \times \boldsymbol{E} = -\boldsymbol{\nabla^2} \boldsymbol{E}. \tag{2.15}$$

Equation(2.13) can be rewritten as vector wave equation for the time-domain electric field as

$$\boldsymbol{\nabla^2} \boldsymbol{E}(\mathbf{r}, \mathtt{t}) - \frac{1}{u^2} \frac{\partial^2}{\partial \mathtt{t}^2} \boldsymbol{E}(\mathbf{r}, \mathtt{t}) = 0, \tag{2.16}$$

where $u^2 = 1/\sqrt{\mu\epsilon}$.

In the spectral domain the above equation reduces to the Helmholtz equation governing the electric field spectrum $E(\mathbf{r})$ [37]

$$\boldsymbol{\nabla^2} \mathbf{E}(\mathbf{r}) + k^2 \mathbf{E}(\mathbf{r}) = 0, \tag{2.17}$$

where $k = \omega\sqrt{\epsilon\mu}$ is the wave number.

2.3 Green's Function

Green's function is the solution of a differential equation with a point source excitation (right-hand-side). Once the solution due to a point source is obtained, the solution due to an arbitrary source is found through superposition as a result of linearity of the differential equation. The overall source is nothing other than a linear superposition of point sources [20].

To demonstrate the Green's function, let's consider an electric potential generated by electric charge q at position $\mathbf{r}'$ in free space, then the electric potential at observation point $\mathbf{r}$ is [21]

$$\phi = \frac{q}{4\pi\epsilon_0|\mathbf{r}-\mathbf{r}'|} \ , \tag{2.18}$$

where ϵ_0 is permittivity of free space and $|\mathbf{r}-\mathbf{r}'|$ indicates the distance between observation point $\mathbf{r}$ and source point $\mathbf{r}'$.

The Green's function is defined as the potential produced by a point source of unit strength, that is

$$G(\mathbf{r},\mathbf{r}') = \frac{1}{4\pi\epsilon_0|\mathbf{r}-\mathbf{r}'|} \ , \tag{2.19}$$

where $G(\mathbf{r},\mathbf{r}')$ is the scalar form of Green's function.

In electromagnetics the source of a field (electric current density) and the field produced by the source (magnetic or electric) are vectors. Each component of the source can produce all three components of the field, this yields nine scalar Green's functions which relate the source (electric or magnetic dipole) to its response (magnetic field or electric field). The compact form of these nine scalar Green's functions is 3×3 matrix introduced as dyadic Green's function. For the electric field produced by the electric dipole (vector point source of unit strength) the dyadic Green's function is the following

$$\overline{\overline{G}}_{e0}(\mathbf{r},\mathbf{r}') = \left(\frac{\boldsymbol{\nabla}\boldsymbol{\nabla}}{k_0^2} + \overline{\overline{I}}\right) G_0(\mathbf{r},\mathbf{r}'), \tag{2.20}$$

where k_0 is the wave number in the vacuum and $\overline{\overline{I}}$ is idem factor (unit dyad).

The magnetic field dyadic Green's function (magnetic field produced by electric dipole of unit strength) in free space is

$$\overline{\overline{G}}_{m0}(\mathbf{r}, \mathbf{r}') = \boldsymbol{\nabla} \times \overline{\overline{G}}_{e0}(\mathbf{r}, \mathbf{r}'). \tag{2.21}$$

2.4 Equivalence Principle

The equivalence principle states that if a particular field exists in a specific region, then different problems can be constructed to produce the same field in that region. The constructed equivalent problem may not have a readily available solution, however, it might provide a variety of approaches to formulate the solution to the original problem [22]. In electromagnetics, the idea of equivalence principle can be extended and applied to complex objects and reduce the complexity of the field finding problem.

The traditional equivalence principle is applied to a region of interest encircled by a closed surface. The equivalent electric and magnetic currents (tangential components of the true magnetic and electric field, respectively) distributed over the closed surface maintain the true fields within the study region while zero fields are produced outside the study region. In the generalized equivalence principle applied to a region of interest, fictitious electric and/or magnetic currents distributed over the closed surface maintain the true fields within the study region while arbitrary (unconstrained) fields are produced outside the study region.

The ability of the equivalence principle to reproduce true field in the region of interest relies on the uniqueness theorem for solution of Maxwell's equations which requires that tangential component of the magnetic field or the electric field are used on the boundary surrounding the region. In the conventional equivalence principle this is obvious, since the equivalent electric and magnetic currents are nothing else

but the tangential components of the true field. In the case of the generalized equivalence principle the currents on the boundary surrounding the region of interest are fictitious current. These fictitious currents, however, are equal to the difference of the tangential components of the true fields inside the region and the bogus field outside of it. However, since the true field tangential components are a part of the fictitious currents, these fictitious currents are able to uniquely reproduce the true field inside the region of interest [13]. Hence, through the uniqueness theorem, generalized equivalence principle, and the boundary conditions, the true fields can be produced within the test region by fictitious currents on it's boundary while auxiliary (bogus) fields are produced outside the region.

2.4.1 Equivalence principle formulation: extinction theorem

Consider the problem in Fig. 2.1 of an object with arbitrary cross-section in a homogeneous medium. The object is excited by incident field $\mathbf{E}^{inc}$ and it has complex relative permittivity and relative magnetic permeability ϵ, μ respectively. The normal vector $\hat{\mathbf{n}}$ points outward from volume V and ∂V is the boundary of that volume.

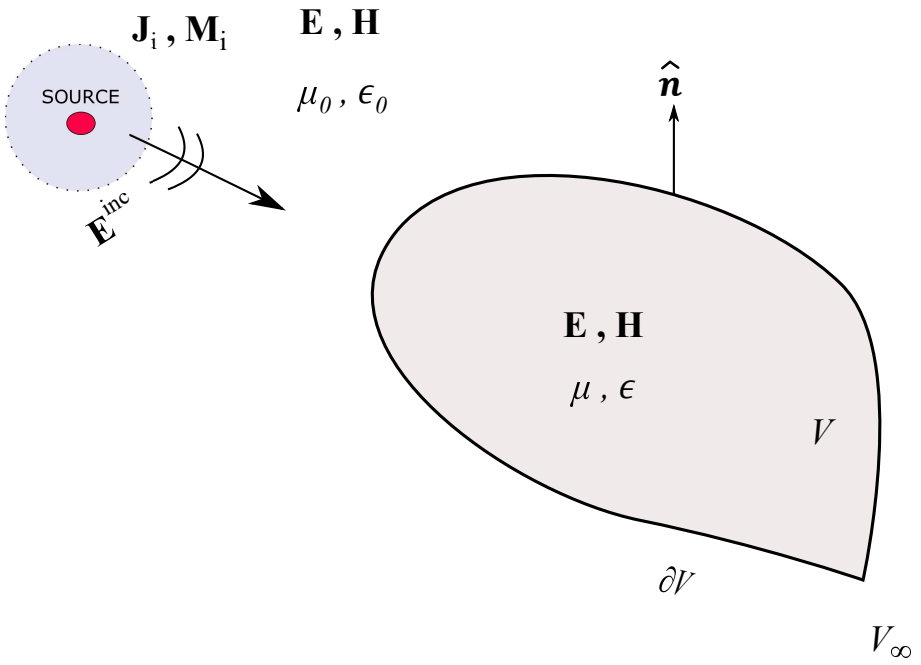

FIGURE 2.1: Scattering problem of an arbitrary object with incident field $\mathbf{E}^{inc}$

The equivalence principle can be applied to develop two models for this problem, one is the equivalent problem of the interior field and the other model is the equivalent problem of the exterior field [12, 23]. The equivalent problem of the interior field is illustrated in Fig. 2.2 where the excitation is provided by impressed magnetic and electric currents $\mathbf{J}_i, \mathbf{M}_i$, and the equivalent sources on the boundary $\mathbf{J}, \mathbf{M}$. These sources radiate in a homogeneous medium with ϵ, μ to produce the scattered fields internal to volume V. The equivalent surface sources are defined as

$$\mathbf{J} = \hat{\mathbf{n}} \times \mathbf{H}, \tag{2.22}$$

$$\mathbf{M} = -\hat{\mathbf{n}} \times \mathbf{E}, \tag{2.23}$$

where the equivalent electric current $\mathbf{J}$ is defined as the tangential component of the true magnetic field on ∂V, while the equivalent magnetic current $\mathbf{M}$ is defined as the tangential component of the true electric field on ∂V.

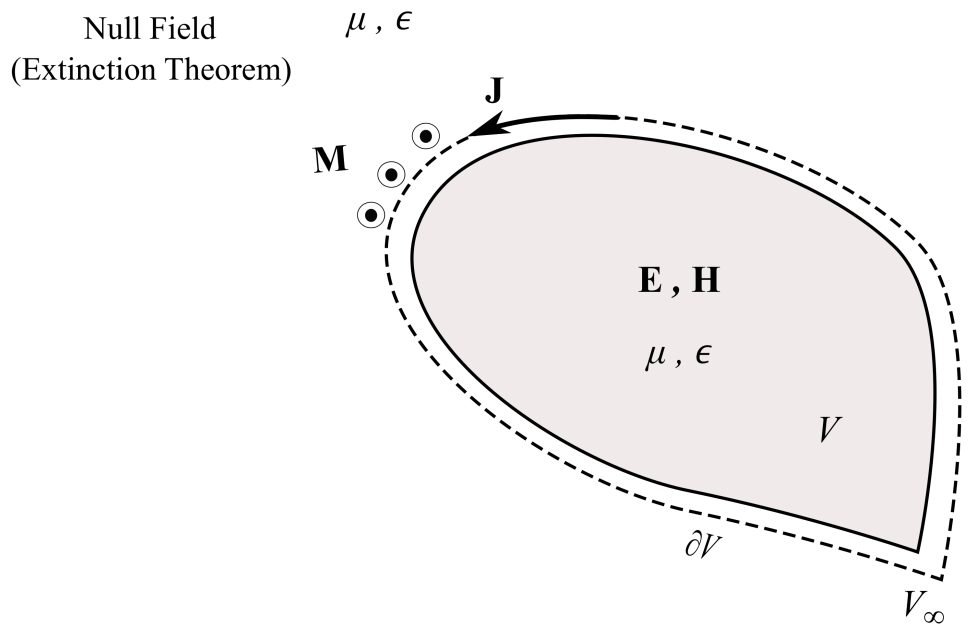

FIGURE 2.2: The equivalent problem of the interior region

The equivalent problem of the exterior field is illustrated in Fig. 2.3. The excitation is provided by impressed magnetic and electric currents $\mathbf{J}_i, \mathbf{M}_i$, and the equivalent sources on the boundary $\mathbf{J}, \mathbf{M}$. Those sources radiate in a homogeneous medium with ϵ_0, μ_0 to produce the scattered fields $\mathbf{E}, \mathbf{H}$ external to V. The equivalent surface sources are defined as

$$\mathbf{J} = \hat{\mathbf{n}} \times \mathbf{H}, \tag{2.24}$$

$$\mathbf{M} = -\hat{\mathbf{n}} \times \mathbf{E}. \tag{2.25}$$

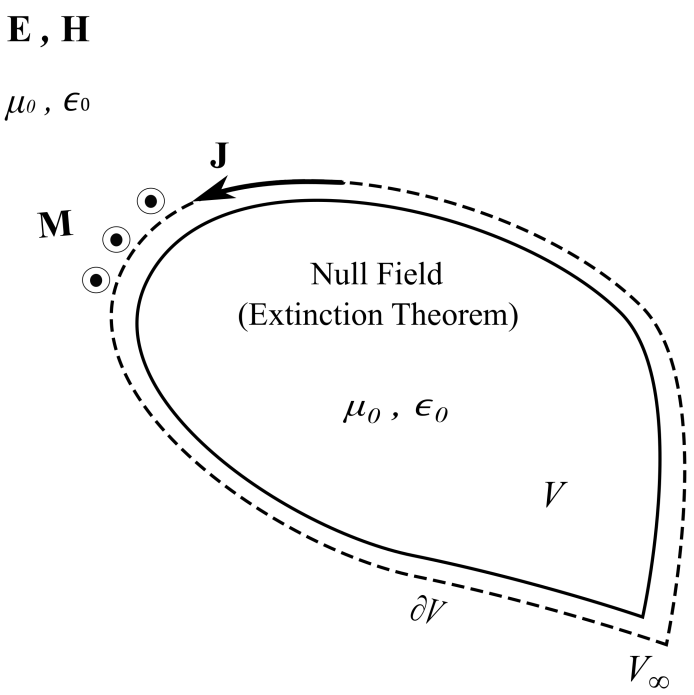

FIGURE 2.3: The equivalent problem of the exterior region

According to [9, 24], the equivalence principle integral representation of the electric field in region V_∞ is demonstrated by application of the second dyadic Green's theorem [25] applied to the volume V_∞ outside the scatterer

$$\begin{aligned} &\mathbf{E}^{inc}(\mathbf{r}) - i\omega\mu_0 \int_{\partial V} \overline{\overline{G}}_{e0}(\mathbf{r},\mathbf{r}') \cdot \mathbf{J}(\mathbf{r}')\, dr' \\ &- \int_{\partial V} \overline{\overline{G}}_{m0}(\mathbf{r},\mathbf{r}') \cdot \mathbf{M}(\mathbf{r}')\, dr' = \begin{cases} \mathbf{E}(\mathbf{r}), & \mathbf{r} \in V_\infty \setminus \partial V, \\ \mathbf{0}, & \mathbf{r} \in V \setminus \partial V, \end{cases} \end{aligned} \tag{2.26}$$

$$\begin{aligned} &\mathbf{H}^{inc}(\mathbf{r}) + \int_{\partial V} \overline{\overline{G}}_{m0}(\mathbf{r},\mathbf{r}') \cdot \mathbf{J}(\mathbf{r}')\, dr' \\ &- i\omega\epsilon_0 \int_{\partial V} \overline{\overline{G}}_{e0}(\mathbf{r},\mathbf{r}') \cdot \mathbf{M}(\mathbf{r}')\, dr' = \begin{cases} \mathbf{H}(\mathbf{r}), & \mathbf{r} \in V_\infty \setminus \partial V, \\ \mathbf{0}, & \mathbf{r} \in V \setminus \partial V, \end{cases} \end{aligned} \tag{2.27}$$

where dyadic Green's functions in region V_∞ satisfies inhomogeneous dyadic wave

equation:

$$\boldsymbol{\nabla} \times \boldsymbol{\nabla} \times \overline{\overline{G}}_{e0}(\mathbf{r}, \mathbf{r}') - \omega^2 \mu_0 \epsilon_0 \overline{\overline{G}}_{e0}(\mathbf{r}, \mathbf{r}') = \overline{\overline{I}} \delta(\mathbf{r}, \mathbf{r}'). \tag{2.28}$$

The magnetic field dyadic Green's function in free space is $\overline{\overline{G}}_{m0} = \boldsymbol{\nabla} \times \overline{\overline{G}}_{e0}$ with relative permittivity ϵ_0 and permeability μ_0.

The equivalence principle integral representation of the electric field in region V is demonstrated by application of the second dyadic Green's theorem applied to the volume V inside the scatterer

$$\begin{aligned} & i\omega\mu \int_{\partial V} \overline{\overline{G}}_{e\epsilon\mu}(\mathbf{r}, \mathbf{r}') \cdot \mathbf{J}(\mathbf{r}') \, dr' \\ & + \int_{\partial V} \overline{\overline{G}}_{m\epsilon\mu}(\mathbf{r}, \mathbf{r}') \cdot \mathbf{M}(\mathbf{r}') \, dr' = \begin{cases} \mathbf{0}, & \mathbf{r} \in V_\infty \setminus \partial V, \\ \mathbf{E}(\mathbf{r}), & \mathbf{r} \in V \setminus \partial V, \end{cases} \end{aligned} \tag{2.29}$$

$$\begin{aligned} & - \int_{\partial V} \overline{\overline{G}}_{m\epsilon\mu}(\mathbf{r}, \mathbf{r}') \cdot \mathbf{J}(\mathbf{r}') \, dr' \\ & + i\omega\epsilon \int_{\partial V} \overline{\overline{G}}_{e\epsilon\mu}(\mathbf{r}, \mathbf{r}') \cdot \mathbf{M}(\mathbf{r}') \, dr' = \begin{cases} \mathbf{0}, & \mathbf{r} \in V_\infty \setminus \partial V, \\ \mathbf{H}(\mathbf{r}), & \mathbf{r} \in V \setminus \partial V, \end{cases} \end{aligned} \tag{2.30}$$

where dyadic Green's functions in region V satisfies inhomogeneous dyadic wave equation:

$$\boldsymbol{\nabla} \times \boldsymbol{\nabla} \times \overline{\overline{G}}_{e\epsilon\mu}(\mathbf{r}, \mathbf{r}') - \omega^2 \mu \epsilon \overline{\overline{G}}_{e\epsilon\mu}(\mathbf{r}, \mathbf{r}') = \overline{\overline{I}} \delta(\mathbf{r}, \mathbf{r}'). \tag{2.31}$$

The previous equations state different forms of equivalence principle integral representation. The exterior equivalence principle is applied to volume V_∞ outside the scatterer where the fields vanish through region V as it is illustrated in (2.26) and (2.27). The right-hand side is zero when observation point is located inside V (extinction theorem). Similarly, when the interior equivalence principle is applied to V inside the scatterer, then null fields are produced in the region V_∞ as it is shown in (2.29) and (2.30). The right-hand side is zero when observation point is located outside V (extinction theorem).

Matching the exterior and interior electric field representation yields the electric

field integral equation (EFIE) while matching the interior and exterior magnetic field representations gives the magnetic field integral equation (MFIE).
The linear combination of electric and magnetic integral equation introduces the combined field integral equation (CFIE).

2.4.2 Generalized equivalence principle

The preceding equivalent principle formulations that are presented in subsection 2.4.1 are a specific case of the generalized equivalent principle representation.
The general form of the equivalence principle has no assumption regarding the material or the fields values outside the study region. The general form can be used to define the fields in an arbitrary region due to surface electric and/or magnetic current. These surface currents are not necessarily the tangential components of the true electric and magnetic field as they are in the traditional equivalence principle. They are equal to the jump of the tangential components of the true electric and magnetic field in the region of interest and unconstrained (bogus) electric and magnetic field outside the region. However, since the tangential component of the true electric and magnetic fields are present in the content of these fictitious surface electric and magnetic currents, the uniqueness theorem still holds and the true electromagnetic field inside the region of interest can be correctly reproduced by such currents [13, 26].
As it was shown earlier, in the traditional equivalence principle applied to the exterior region (2.26) and (2.27) the electric and magnetic fields inside scatterer vanish (by extinction theorem). In the generalized equivalence principle the field inside the scattered can be arbitrary while outside being the true field and represented by the fictitious electric and magnetic surface currents as

$$\begin{aligned}
&\mathbf{E}^{inc}(\mathbf{r}) - i\omega\mu_0 \int\limits_{\partial V} \overline{\overline{G}}_{e0}(\mathbf{r},\mathbf{r}') \cdot \boldsymbol{\mathcal{J}}(\mathbf{r}')\ dr' \\
&- \int\limits_{\partial V} \overline{\overline{G}}_{m0}(\mathbf{r},\mathbf{r}') \cdot \boldsymbol{\mathcal{M}}(\mathbf{r}')\ dr' = \begin{cases} \mathbf{E}(\mathbf{r}), & \mathbf{r} \in V_\infty \setminus \partial V, \\ \mathbf{E}_{in}(\mathbf{r}), & \mathbf{r} \in V \setminus \partial V, \end{cases}
\end{aligned} \tag{2.32}$$

$$\begin{aligned}
&\mathbf{H}^{inc}(\mathbf{r}) + \int\limits_{\partial V} \overline{\overline{G}}_{m0}(\mathbf{r},\mathbf{r}') \cdot \boldsymbol{\mathcal{J}}(\mathbf{r}')\ dr' \\
&- i\omega\epsilon_0 \int\limits_{\partial V} \overline{\overline{G}}_{e0}(\mathbf{r},\mathbf{r}') \cdot \boldsymbol{\mathcal{M}}(\mathbf{r}')\ dr' = \begin{cases} \mathbf{H}(\mathbf{r}), & \mathbf{r} \in V_\infty \setminus \partial V, \\ \mathbf{H}_{in}(\mathbf{r}), & \mathbf{r} \in V \setminus \partial V. \end{cases}
\end{aligned} \tag{2.33}$$

The equivalent currents defined on the boundary are not unique unless Maxwellian electric and magnetic fields are specified internal to region V, then fictitious electric current $\boldsymbol{\mathcal{J}}$ is uniquely defined to be the difference between the tangential component of the true field outside the scatterer and the arbitrary Maxwellian magnetic field $\mathbf{H}_{in}$ that is specified inside scatterer. Similarly, the fictitious magnetic current $\boldsymbol{\mathcal{M}}$ is defined to be the difference between the tangential component of the true field outside the scatterer and the arbitrary Maxwellian electric field $\mathbf{E}_{in}$ that is specified inside scatterer [23]. The equivalent surface sources are defined as

$$\boldsymbol{\mathcal{J}} = \hat{\mathbf{n}} \times (\mathbf{H} - \mathbf{H}_{in}), \tag{2.34}$$

$$\boldsymbol{\mathcal{M}} = (\mathbf{E} - \mathbf{E}_{in}) \times \hat{\mathbf{n}}. \tag{2.35}$$

The interior equivalent integral forms in (2.29) and (2.30) force the electric and magnetic fields outside scatterer to vanish, while it can be allowed to be arbitrary. Hence, the following equivalent integral representations are obtained:

$$\begin{aligned}
&i\omega\mu \int\limits_{\partial V} \overline{\overline{G}}_{e\epsilon\mu}(\mathbf{r},\mathbf{r}') \cdot \boldsymbol{\mathcal{J}}(\mathbf{r}')\ dr' \\
&+ \int\limits_{\partial V} \overline{\overline{G}}_{m\epsilon\mu}(\mathbf{r},\mathbf{r}') \cdot \boldsymbol{\mathcal{M}}(\mathbf{r}')\ dr' = \begin{cases} \mathbf{E}_{out}(\mathbf{r}), & \mathbf{r} \in V_\infty \setminus \partial V, \\ \mathbf{E}(\mathbf{r}), & \mathbf{r} \in V \setminus \partial V, \end{cases}
\end{aligned} \tag{2.36}$$

$$
\begin{aligned}
&-\int_{\partial V} \overline{\overline{G}}_{m\epsilon\mu}(\mathbf{r},\mathbf{r}') \cdot \boldsymbol{\mathcal{J}}(\mathbf{r}')\ dr' \\
&+ i\omega\epsilon \int_{\partial V} \overline{\overline{G}}_{e\epsilon\mu}(\mathbf{r},\mathbf{r}') \cdot \boldsymbol{\mathcal{M}}(\mathbf{r}')\ dr' = \begin{cases} \mathbf{H}_{out}(\mathbf{r}), & \mathbf{r} \in V_\infty \setminus \partial V, \\ \mathbf{H}(\mathbf{r}), & \mathbf{r} \in V \setminus \partial V. \end{cases}
\end{aligned} \tag{2.37}
$$

Analogously, the equivalent currents defined on the boundary are not unique unless Maxwellian electric and magnetic fields are specified external to region V, then fictitious electric current $\boldsymbol{\mathcal{J}}$ is uniquely defined to be the difference between the tangential component of the true field $\mathbf{H}$ inside the scatterer and the arbitrary Maxwellian magnetic field $\mathbf{H}_{out}$ that is specified outside scatterer. Similarly, the fictitious magnetic current $\boldsymbol{\mathcal{M}}$ is defined to be the difference between the tangential component of the true field $\mathbf{E}$ inside the scatterer and the arbitrary Maxwellian electric field $\mathbf{E}_{out}$ that is specified outside scatterer [23]. The equivalent surface sources are defined as

$$\boldsymbol{\mathcal{J}} = \hat{\mathbf{n}} \times (\mathbf{H}_{out} - \mathbf{H}), \tag{2.38}$$

$$\boldsymbol{\mathcal{M}} = (\mathbf{E}_{out} - \mathbf{E}) \times \hat{\mathbf{n}}. \tag{2.39}$$

2.5 Volume Equivalence Principle

Consider an object that is characterized by permittivity ϵ and permeability μ, where an electric current source and magnetic current source are radiating in the presence of that object. Both the source and the object are situated in free space with constant permittivity ϵ_0 and permeability μ_0. The electric and magnetic fields radiating from the source satisfy Maxwell's equations [9, 22], as follows:

$$\nabla \times \mathbf{E}(\mathbf{r}) = -i\omega\mu(\mathbf{r})\mathbf{H}(\mathbf{r}) - \mathbf{M}(\mathbf{r}), \tag{2.40}$$

$$\nabla \times \mathbf{H}(\mathbf{r}) = i\omega\epsilon(\mathbf{r})\mathbf{E}(\mathbf{r}) + \mathbf{J}(\mathbf{r}), \tag{2.41}$$

where $\mu(\mathbf{r})$ and $\epsilon(\mathbf{r})$ denote the position-dependent permittivity and permeability.

The solution of above equations can not be obtained easily since the permittivity and permeability are changing throughout the entire space, and they are not constant. Therefore, it is convenient to represent scattering problem into an equivalent problem where the dielectric and magnetic materials are replaced by equivalent polarization electric and magnetic currents $\boldsymbol{j}(\mathbf{r})$ and $\boldsymbol{m}(\mathbf{r})$, respectively, [9]. Equations (2.40) and (2.41) can be rewritten as

$$\boldsymbol{\nabla} \times \mathbf{E}(\mathbf{r}) = -i\omega\mu_0 \mathbf{H}(\mathbf{r}) - \boldsymbol{m}(\mathbf{r}) - \mathbf{M}(\mathbf{r}), \tag{2.42}$$

$$\boldsymbol{\nabla} \times \mathbf{H}(\mathbf{r}) = i\omega\epsilon_0 \mathbf{E}(\mathbf{r}) + \boldsymbol{j}(\mathbf{r}) + \mathbf{J}(\mathbf{r}), \tag{2.43}$$

where

$$\boldsymbol{m}(\mathbf{r}) = i\omega \left[\mu(\mathbf{r}) - \mu_0\right] \mathbf{H}(\mathbf{r}), \tag{2.44}$$

$$\boldsymbol{j}(\mathbf{r}) = i\omega \left[\epsilon(\mathbf{r}) - \epsilon_0\right] \mathbf{E}(\mathbf{r}). \tag{2.45}$$

The process of replacing the effect of the dielectric and magnetic materials by induced sources $\boldsymbol{j}$ and $\boldsymbol{m}$ that exist only in the volume of the object is referred to as the volumetric equivalence principle.

According to [22] the volumetric equivalence principle, the electric and magnetic fields are produced according to superposition by the volume polarization currents $\boldsymbol{j}$ and $\boldsymbol{m}$ occupying object's volume V_o and extraneous (impressed) currents $\mathbf{J}$, $\mathbf{M}$ occupying source V_s, both radiating in free-space

$$\begin{aligned} \mathbf{E}(\mathbf{r}) = &-i\omega\mu_0 \int_{V_s} \overline{\overline{G}}_{e0}(\mathbf{r}, \mathbf{r}') \cdot \mathbf{J}(\mathbf{r}')\, dV' - \int_{V_s} \overline{\overline{G}}_{m0}(\mathbf{r}, \mathbf{r}') \cdot \mathbf{M}(\mathbf{r}')\, dV' \\ &- i\omega\mu_0 \int_{V_o} \overline{\overline{G}}_{e0}(\mathbf{r}, \mathbf{r}') \cdot \boldsymbol{j}(\mathbf{r}')\, dV' - \int_{V_o} \overline{\overline{G}}_{m0}(\mathbf{r}, \mathbf{r}') \cdot \boldsymbol{m}(\mathbf{r}')\, dV', \end{aligned} \tag{2.46}$$

$$\begin{aligned}\mathbf{H}(\mathbf{r}) = &\int_{V_s} \overline{\overline{G}}_{m0}(\mathbf{r},\mathbf{r}') \cdot \mathbf{J}(\mathbf{r}')\ dV' - i\omega\epsilon_0 \int_{V_s} \overline{\overline{G}}_{e0}(\mathbf{r},\mathbf{r}') \cdot \mathbf{M}(\mathbf{r}')\ dV' \\ &+ \int_{V_o} \overline{\overline{G}}_{m0}(\mathbf{r},\mathbf{r}') \cdot \boldsymbol{j}(\mathbf{r}')\ dV' - i\omega\epsilon_0 \int_{V_o} \overline{\overline{G}}_{e0}(\mathbf{r},\mathbf{r}') \cdot \boldsymbol{m}(\mathbf{r}')\ dV'.\end{aligned} \tag{2.47}$$

The first and the second terms in (2.46) and (2.47) represent the incident fields $\mathbf{E}^{inc}$ and $\mathbf{H}^{inc}$ is produced by $\mathbf{M}$ and $\mathbf{J}$. With these notations for the incident field, the volume equivalence principle field representations have the form

$$\mathbf{E}(\mathbf{r}) = \mathbf{E}^{inc}(\mathbf{r}) - i\omega\mu_0 \int_{V_o} \overline{\overline{G}}_{e0}(\mathbf{r},\mathbf{r}') \cdot \boldsymbol{j}(\mathbf{r}')\ dV' - \int_{V_o} \overline{\overline{G}}_{m0}(\mathbf{r},\mathbf{r}') \cdot \boldsymbol{m}(\mathbf{r}')\ dV' \tag{2.48}$$

$$\mathbf{H}(\mathbf{r}) = \mathbf{H}^{inc}(\mathbf{r}) + \int_{V_o} \overline{\overline{G}}_{m0}(\mathbf{r},\mathbf{r}') \cdot \boldsymbol{j}(\mathbf{r}')\ dV' - i\omega\epsilon_0 \int_{V_o} \overline{\overline{G}}_{e0}(\mathbf{r},\mathbf{r}') \cdot \boldsymbol{m}(\mathbf{r}')\ dV' \tag{2.49}$$

where $\mathbf{r}$ is an arbitrary observation point location in space which can be inside the object, on its boundary, outside the object, or in the region of sources V_s.

2.6 Single-Source Integral Equation

The surface integral equations mentioned previously are formulated with respect to two unknown current densities. A single source surface integral equations (SSIE) are formulated with respect to a single unknown current density instead.

The ambiguity in the definition of auxiliary fields in (2.32) leads the fictitious equivalent electric current $\boldsymbol{\mathcal{J}}$ and the fictitious equivalent magnetic current $\boldsymbol{\mathcal{M}}$, which can related as $\boldsymbol{\mathcal{J}} = a\boldsymbol{\mathcal{J}}_0$ and $\boldsymbol{\mathcal{M}} = b\hat{\mathbf{n}} \times \boldsymbol{\mathcal{J}}_0$, where a and b are arbitrary constants [13, 28, 29].

Substituting the single fictitious current into the general representation of exterior equivalence principle (2.32) and (2.33) yields single-source field representation in region V_∞ that is

$$\begin{aligned}
&\mathbf{E}^{inc}(\mathbf{r}) - i\omega\mu_0 \int\limits_{\partial V} \overline{\overline{G}}_{e0}(\mathbf{r},\mathbf{r}') \cdot a\boldsymbol{\mathcal{J}}_0(\mathbf{r}')\ dr' \\
&- \int\limits_{\partial V} \overline{\overline{G}}_{m0}(\mathbf{r},\mathbf{r}') \cdot b\hat{\mathbf{n}} \times \boldsymbol{\mathcal{J}}_0(\mathbf{r}')\ dr' = \begin{cases} \mathbf{E}(\mathbf{r}), & \mathbf{r} \in V_\infty \setminus \partial V, \\ \mathbf{E}_{in}(\mathbf{r}), & \mathbf{r} \in V \setminus \partial V, \end{cases}
\end{aligned} \tag{2.50}$$

$$\begin{aligned}
&\mathbf{H}^{inc}(\mathbf{r}) + \int\limits_{\partial V} \overline{\overline{G}}_{m0}(\mathbf{r},\mathbf{r}') \cdot a\boldsymbol{\mathcal{J}}_0(\mathbf{r}')\ dr' \\
&- i\omega\epsilon_0 \int\limits_{\partial V} \overline{\overline{G}}_{e0}(\mathbf{r},\mathbf{r}') \cdot b\hat{\mathbf{n}} \times \boldsymbol{\mathcal{J}}_0(\mathbf{r}')\ dr' = \begin{cases} \mathbf{H}(\mathbf{r}), & \mathbf{r} \in V_\infty \setminus \partial V, \\ \mathbf{H}_{in}(\mathbf{r}), & \mathbf{r} \in V \setminus \partial V. \end{cases}
\end{aligned} \tag{2.51}$$

In the same manner, upon substitution into the generalized representation of interior equivalent field (2.36) and (2.37) for $\boldsymbol{\mathcal{J}}$ and $\boldsymbol{\mathcal{M}}$ in terms of single fictitious current, the single-source field representation in region V is expressed as follows:

$$\begin{aligned}
&i\omega\mu \int\limits_{\partial V} \overline{\overline{G}}_{e\epsilon\mu}(\mathbf{r},\mathbf{r}') \cdot a\boldsymbol{\mathcal{J}}_0(\mathbf{r}')\ dr' \\
&+ \int\limits_{\partial V} \overline{\overline{G}}_{m\epsilon\mu}(\mathbf{r},\mathbf{r}') \cdot b\hat{\mathbf{n}} \times \boldsymbol{\mathcal{J}}_0(\mathbf{r}')\ dr' = \begin{cases} \mathbf{E}_{out}(\mathbf{r}), & \mathbf{r} \in V_\infty \setminus \partial V, \\ \mathbf{E}(\mathbf{r}), & \mathbf{r} \in V \setminus \partial V, \end{cases}
\end{aligned} \tag{2.52}$$

$$\begin{aligned}
&- \int\limits_{\partial V} \overline{\overline{G}}_{m\epsilon\mu}(\mathbf{r},\mathbf{r}') \cdot a\boldsymbol{\mathcal{J}}_0(\mathbf{r}')\ dr' \\
&+ i\omega\epsilon \int\limits_{\partial V} \overline{\overline{G}}_{e\epsilon\mu}(\mathbf{r},\mathbf{r}') \cdot b\hat{\mathbf{n}} \times \boldsymbol{\mathcal{J}}_0(\mathbf{r}')\ dr' = \begin{cases} \mathbf{H}_{out}(\mathbf{r}), & \mathbf{r} \in V_\infty \setminus \partial V, \\ \mathbf{H}(\mathbf{r}), & \mathbf{r} \in V \setminus \partial V. \end{cases}
\end{aligned} \tag{2.53}$$

Chapter 3

Surface-Volume-Surface Electric Field Integral Equation (SVS-EFIE)

3.1 SVS-EFIE: Introduction

The Surface-Volume-Surface Electric Field Integral Equation (SVS-EFIE), which is a new class of single-source surface integral equations, was introduced in [14] for electromagnetic scattering problems on homogeneous non-magnetic scatterers and imperfect 3-D conductors. Prior 2-D formulations of SVS-EFIE and their MoM [21] solutions were developed in [30, 31].

The new single-source integral equation is obtained by constraining the single-source field representations with the the traditional volumetric equivalence principle as opposed to the surface equivalence principle as it was done previously [13]. The classical volume integral equation produces the new single-source equation through its enforcement on the boundary instead of volume of the scatterer while the field inside the scatterer is represented using only a fictitious electric surface current in the

generalized equivalence principle. Such single-source field representation can also be viewed as a mere superposition of spherical waves emanating from the boundary of the scatterer and weighed with the fictitious surface current.

In the traditional SSIE, the unknown current density is constrained by substituting its single-source integral field representation into the classical surface equivalence principle, producing the needed constraining for the unknown fictitious surface current density.
In SVS-EFIE, on the other hand, the unknown current density in the single-source field representation is constrained through its substitution into the classical volume equivalence theorem and enforcing the latter only on the boundary of the scatterer and only for the tangential component of the field. Instead of being enforced volume integral equation throughout the entire volume of the scatterer it is only enforced for the tangential component of the total electric field and only on the boundary since the unknown fictitious current density is a surface function which is tangential to the boundary of the scatterer [14].

The resultant equation has several advantages in comparison with the traditional surface integral equations. In case of SVS-EFIE formulation for the composite objects there are no complications in handling material junctions [32] as it is encountered in the traditional SIE formulations [33]. It has only electric current density on the surface of the scatterer as opposed to both electric and magnetic current densities featured in the traditional SIEs. SVS-EFIE also has only one integral operator product. In addition, it has only electric field Green's functions which is beneficial in case of solving scattering problems on objects located in multi-layered media [15] . Furthermore, accelerating SVS-EFIE with the FFT-based fast algorithms yields the same CPU memory and time complexity as the solution of either classical SIEs or SSIEs [14].

3.2 SVS-EFIE Formulation

Using the volumetric equivalence principle (2.48) the total electric field $\mathbf{E}$ inside a volume V of a homogeneous non-magnetic dielectric or imperfect-conductor object ($\mu = \mu_0$) is expressed as

$$\mathbf{E} = \mathbf{E}^{\text{inc}}(\mathbf{r}) + k_0^2 \left(\epsilon_r - 1\right) \int_V \overline{\overline{G}}_{e0}(\mathbf{r}, \mathbf{r}') \cdot \mathbf{E}(\mathbf{r}') \, dV', \tag{3.1}$$

where $k_0 = \omega\sqrt{\epsilon_o \mu_0}$ is the wave number of vacuum and ϵ_r is the complex relative permittivity

$$\epsilon_r = \varepsilon_r \left[1 + \frac{\sigma}{i\omega\varepsilon_r\varepsilon_0}\right], \tag{3.2}$$

ε_r is relative permittivity and σ is the bulk conductivity of the object material.

The electric field inside the scatterer's volume satisfies the homogeneous wave equation

$$\boldsymbol{\nabla} \times \boldsymbol{\nabla} \times \mathbf{E}(\mathbf{r}) - k_\epsilon^2 \mathbf{E}(\mathbf{r}) = \mathbf{0}, \quad \mathbf{r} \in V \setminus \partial V. \tag{3.3}$$

The total electric field $\mathbf{E}$ can be written as a superposition of waves contribution emanating from the source points on the object boundary ∂V

$$\mathbf{E}(\mathbf{r}) = -i\omega\mu_0 \oint_{\partial V} \overline{\overline{G}}_{e\epsilon}(\mathbf{r}, \mathbf{r}') \cdot \boldsymbol{\mathcal{J}}(\mathbf{r}') \, dS', \quad \mathbf{r} \in V \backslash \partial V, \tag{3.4}$$

where $\overline{\overline{G}}_{e\epsilon}(\mathbf{r}, \mathbf{r}')$ is the Green's function of homogeneous space with the material properties of the non-magnetic object of interest, which satisfies the following homogeneous wave equation

$$\boldsymbol{\nabla} \times \boldsymbol{\nabla} \times \overline{\overline{G}}_{e\epsilon} - k_\epsilon^2 \overline{\overline{G}}_{e\epsilon} = \overline{\overline{\mathbf{0}}}, \tag{3.5}$$

where $k_\epsilon = k_0\sqrt{\epsilon_r}$.

The waves emanating from the boundary of scatterer are weighted by the unknown

fictitious electric current density $\boldsymbol{\mathcal{J}}$ which is defined on the scatterer boundary ∂V. The substitution of (3.4) into (3.1) followed by the restriction of the observation domain to ∂V yields SVS-EFIE, that is

$$\begin{aligned} i\omega\mu_0\hat{\mathbf{t}}\cdot\Bigg(&-\oint_{\partial V}\overline{\overline{G}}_{e\epsilon}(\mathbf{r},\boldsymbol{r}'')\cdot\boldsymbol{\mathcal{J}}(\boldsymbol{r}'')\;dS''+k_0^2\left(\epsilon_r-1\right)\\ &\int_V\overline{\overline{G}}_{e0}(\mathbf{r},\mathbf{r}')\cdot\oint_{\partial V}\overline{\overline{G}}_{e\epsilon}(\mathbf{r}',\boldsymbol{r}'')\cdot\boldsymbol{\mathcal{J}}(\boldsymbol{r}'')\;dS''dV'\Bigg)\\ &=\hat{\mathbf{t}}\cdot\mathbf{E}^{\text{inc}}(\mathbf{r}),\quad \mathbf{r}\in\partial V, \end{aligned} \tag{3.6}$$

where $\hat{\mathbf{t}}$ is the tangential vector to the boundary ∂V.

The SVS-EFIE formulation can be rewritten in more compact convenient form by using the integral operators as [14]

$$-\overline{\overline{\mathcal{T}}}_{\epsilon}^{\partial V,\partial V}\circ\boldsymbol{\mathcal{J}}+\overline{\overline{\mathcal{T}}}_{0}^{\partial V,V}\circ\overline{\overline{\mathcal{T}}}_{\epsilon}^{V,\partial V}\circ\boldsymbol{\mathcal{J}}=\hat{\mathbf{t}}\cdot\mathbf{E}^{inc}(\mathbf{r}) \tag{3.7}$$

3.3 SVS-EFIE Discretization

The MoM [8, 21] is a powerful computational technique and it is applied to wide variety of practical electromagnetic problems that can not be solved analytically. The goal of MoM is to reduce a given integral equations to a system of linear algebraic equations, which can subsequently be solved numerically using a known techniques.

The process of applying MoM to solution of an integral equation in electromagnetics requires the following steps:

1. Discretization (expansion) of the unknown current using known (typically simpler) basis functions,

2. Substitution of discretized unknown current into the IE to obtain the discretized form of IE,

3. Testing the discretized IE with known test functions (often taken to be the same as basis functions),

4. Computation of matrix entries through evaluation of the interactions between basis functions and test functions, and

5. Solving the linear system of algebraic equations in order to obtain the sought coefficients in the expansion of the unknown current.

The numerical solution of SVS-EFIE with MoM is described in details in [14] and briefly outlined here. The MoM solution requires 3-D mesh that discretizes the scatterer volume V with N tetrahedral elements. It also requires 2-D mesh that discretizes the scatterer surface ∂V with M triangle elements, see Fig. 3.1. The constructed mesh is a discrete representation of the geometry that is utilized to solve a given scattering or radiation problem.

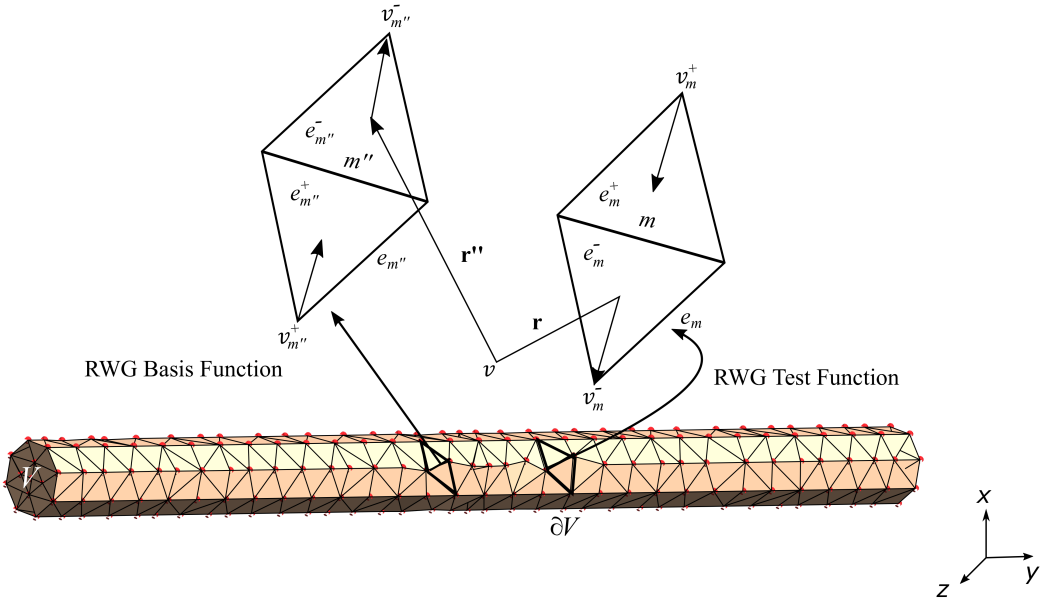

FIGURE 3.1: The 3-D mesh discretizing the volume V with tetrahedral elements and 2-D mesh discretizing the boundary surface ∂V with triangle elements. RWG basis and test functions defined on the surface triangles are also shown.

In order to solve SVS-EFIE numerically via MoM, the unknown fictitious electric current density $\boldsymbol{\mathcal{J}}$ on ∂V is discretized into a set of P basis functions, that is

$$\boldsymbol{\mathcal{J}}(\boldsymbol{r}'') \cong \sum_{m''=1}^{P} I_{m''} \boldsymbol{t}_{m''}(\boldsymbol{r}''), \tag{3.8}$$

where $\boldsymbol{t}_{m''}$ is the RWG basis function [21] that is defined on the m''th common edge between adjacent surface triangles, $I_{m''}$ are the unknown coefficients in the unknown current expansion, and P is the total number of RWG basis.

After unknown current density is expanded into RWG basis functions, the testing of the SVS-EFIE is performed with the same set of RWG functions (Galerkin MoM [34]).
The discretization of SVS-EFIE via MoM yields a set of linear algebraic equations with respect to unknown coefficients $I_1, ..., I_P$. After solving the system of linear equations, the electric field $\mathbf{E}$ and volume polarization current $\boldsymbol{j}$ inside V can be computed using the single-source representation (3.4) which is can be viewed as a superposition of the waves emanating from ∂V and weighed by $\boldsymbol{\mathcal{J}}$.

Further details about SVS-EFIE formulation and the discretization of each operator of the equation is presented in [14].

Chapter 4

Delta-Gap Excitation Mechanism

4.1 Introduction

The antenna comprises a metalic object for receiving or radiating waves [38]. There are various types of antennas such as wire antennas, microstrip antennas, array antennas, etc. The wire antennas are the most popular type due to their simplicity in construction.

The solution of radiation or scattering problem for antenna system can be obtained by the integral equation method where the unknown quantity is cast into the integral equation form. The solution of the integral equation is determined by one of the numerical techniques which is developed in order to perform an accurate analysis and proper design for the antenna system. The performance of antenna can be described by specifying various parameters such as radiation pattern, gain, input impedance, etc. In this work we are interested in the input impedance at the input terminals of the antenna as it plays an essential role in antenna and transmission line design, also it is used to determine the efficiency of the antenna . Matching the input impedance of the antenna with the characteristic impedance of the transmission line leads to minimizing the losses of energy in the process of field radiation.

The input impedance is the impedance defined at the antenna's terminals as the ratio of the voltage to the current at that point. The input impedance is expressed as

$$Z_A = R_A + jX_A, \tag{4.1}$$

where the resistive part R_A consists of two components: the radiation resistance R_r that represents the power delivered to the antenna for radiation and the loss resistance of the antenna R_L that represents the power dissipated as heat.

The antenna can be represented by an equivalent circuit shown in Fig. 4.1.

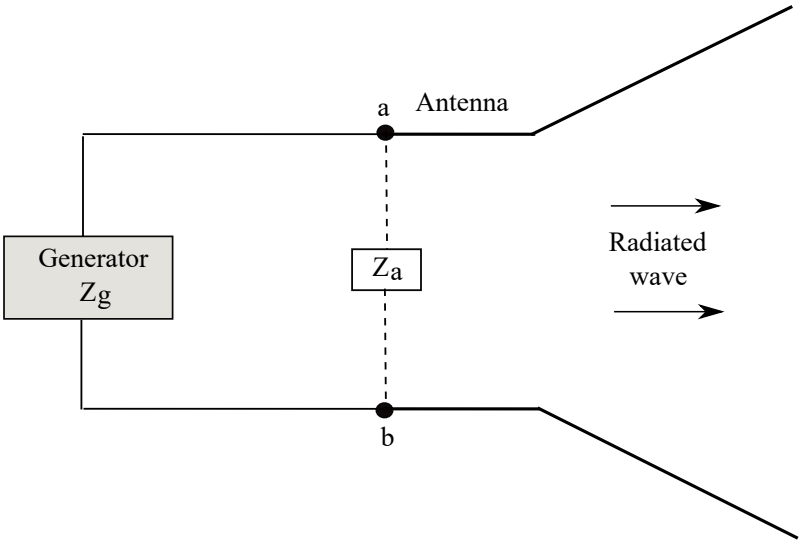

FIGURE 4.1: Equivalent circuit of transmitting antenna.

The input impedance can be calculated by solving an integral equation using a numerical technique. After the current distribution is obtained from the MoM solution of the integral equation, the input impedance is found using the ratio of the voltage at the feed terminals to the current, that is

$$Z_{in} = \frac{V_{in}}{I_{in}}. \tag{4.2}$$

4.2 Methods for Excitation Modeling of Antenna

The behavior of electromagnetic fields produced by an antenna is governed either by the integral or the differential equations. The numerical solution of such equations requires an excitation model at the input terminals of the antenna under consideration.

In the integral equation formulations, typically, two excitation models are used. One such model is the delta-gap source and the other is the magnetic frill source [38]. Apart from these traditional models, there are other models for driving the antennas. These are rarely used, however, due to their complexity.

In this work, delta-gap excitation mechanism is used to feed a cylindrical dipole where the width of the gap tends to zero. The antenna analysis is performed by obtaining the input impedance and the radiation pattern from the current distribution defined on the antenna surface when the voltage is known at the feed terminals of the antenna.

The excitation method used in this work is commonly referred to as the 'delta-gap' source model, where the term "gap" denotes the voltage source region. Term "delta" refers to the delta function which describes the electric field as a function of position in the gap, that is

$$\mathbf{E}^{inc} = \lim_{\Delta \to 0} \frac{V}{\Delta} \hat{\mathbf{p}} = V \ \delta(p - p_0) \hat{\mathbf{p}}, \tag{4.3}$$

where Δ is the width of the gap, p is the coordinate along direction of the electric field in the gap, i.e. $p \in [-\Delta/2, \Delta/2]$, p_0 is location of the center of the gap along coordinate p, $\hat{\mathbf{p}}$ is unit vector along coordinate p, δ is Dirac's delta-function.

The delta-gap source model has been used extensively due to its simplicity and

wide range of applications [4]. When delta-gap source model is used in EFIE formulation, the incident field over the gap feed is described by (4.3), to signify the impressed unit voltage applied across the feed terminal of the antenna. The EFIE with the delta-gap excitation models can be discretized using the MoM with RWG basis functions, see Fig. 4.7.

In this work we extend the concept of delta-gap source model to the SVS-EFIE. The SVS-EFIE is discretized via MoM using RWG basis functions similarly with the discretization of the EFIE. The numerical solution of the resultant linear system of equations yields the total electric field across the gap which in turn allows us to determine the input impedance of the antenna driven by the delta-gap source model.

4.3 Magnetic Frill Source Model

The magnetic frill model was introduced to compute the near and far zone fields from coaxial aperture [38]. In this model, the feed gap is replaced with a magnetic current density $\mathbf{M}$ that exists over the annular aperture with an inner radius a and outer radius b as shown in Fig. 4.2. The inner radius is usually chosen to be the radius of the wire. The circularly directed magnetic current induces an electric field on the axis of the wire that feeds the antenna [38].

A particular model of the magnetic frill generator can be considered by letting the radius b tends to radius a, $(b \to a)$. This small frill generator is called a magnetic current loop source which was recently introduced for thin wire antenna applications [39, 40].

In the special limiting case when $(a \to 0)$, the small frill generator is reduced to the delta-gap source where the magnetic current degenerates into an infinitesimally thin ring. The electric field impressed over the feed region exhibits the properties of the delta function. [39].

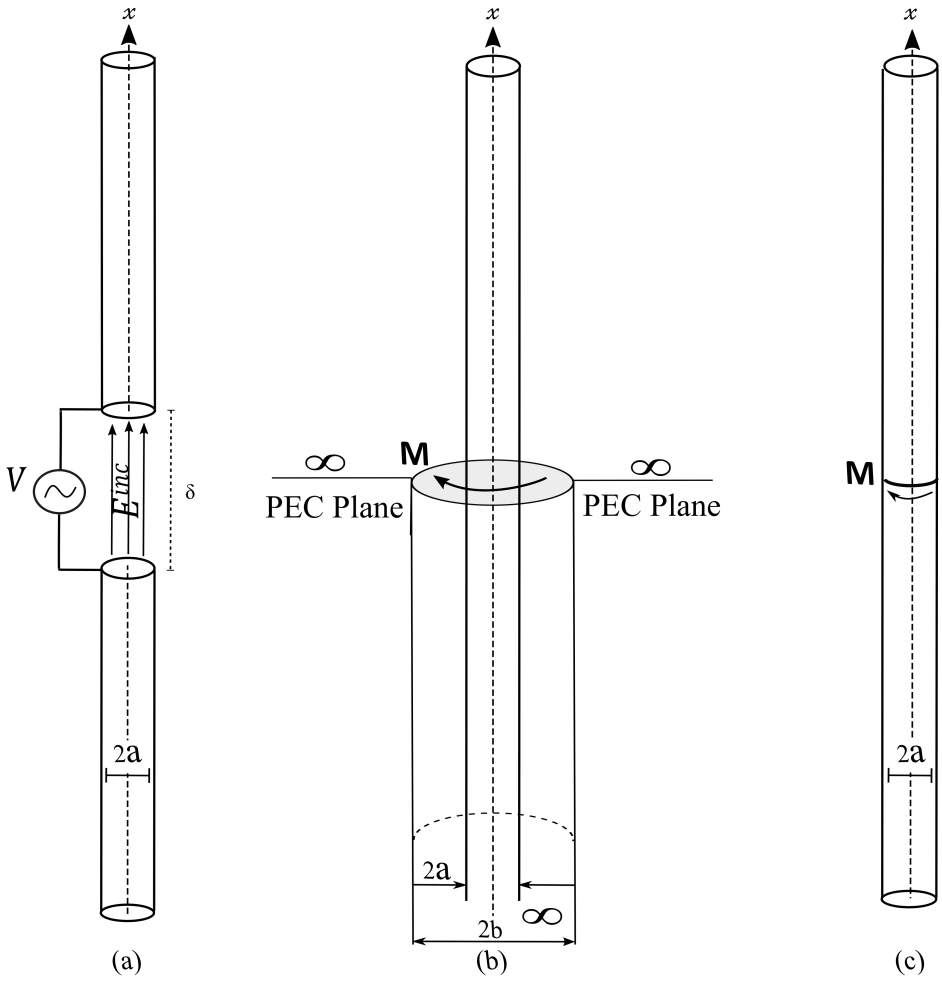

FIGURE 4.2: The excitation methods of the antenna: (a) Delta-gap, (b) Magnetic frill, (c) Magnetic current loop.

In order to use the magnetic current loop source in EFIE, a PEC dipole antenna is considered. The gap between the antenna input terminals is filled with PEC material and surrounded by **M**, as shown in Fig. 4.3. This generates an electric field, which becomes the incident field for EFIE formulation.

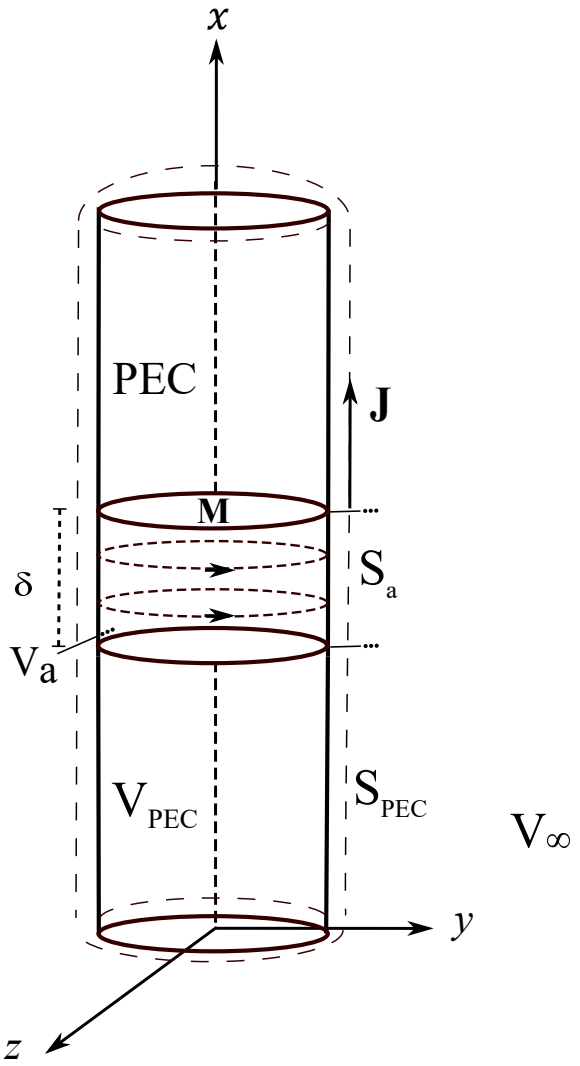

FIGURE 4.3: An equivalent problem of perfect electric conductor (PEC) used for magnetic frill current modeling.

If the gap is much smaller than the wavelength, **M** can be assumed to be uniform (constant along the gap direction) and analogous to the magnetic current of a finite-length solenoid [6]. For an infinitely long solenoid, the field inside the coil is known to be uniform, while it is zero outside [41]. The infinite solenoid structure of the field approximates the field in the solenoid of the finite length and, hence, the field of the uniform **M** circulating around the gap filled with PEC in the magnetic current source model. This implies that the impressed incident field inside the PEC-filled-gap is close to being uniformly distributed and it is close zero outside in the near

vicinity of **M**.

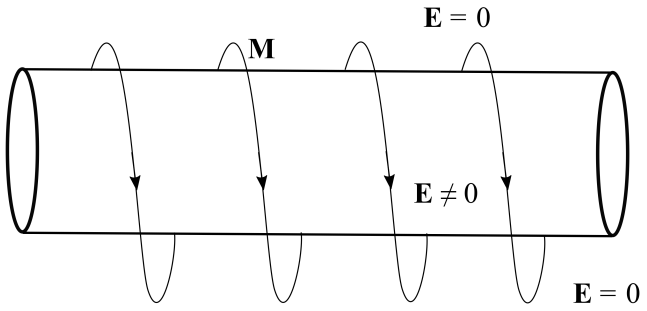

FIGURE 4.4: Uniformly distributed field inside a long solenoid.

Applying the exterior equivalence principle to the volume outside the dipole region V_{PEC}, we can express the total electric field outside the PEC region in terms of the equivalent electric and magnetic currents, as follows:

$$\mathbf{E}(\mathbf{r}) = i\omega\mu_0 \int\limits_{S_{PEC}} \overline{\overline{G}}_{e0}(\mathbf{r},\mathbf{r}') \cdot \mathbf{J}(\mathbf{r}')\ dS' + \int\limits_{S_a} \overline{\overline{G}}_{m0}(\mathbf{r},\mathbf{r}') \cdot \mathbf{M}(\mathbf{r}')\ dS', \quad \mathbf{r} \in V_\infty, \quad (4.4)$$

The equivalent surface encloses PEC region. Thus, the tangential component of the total electric field on PEC surface is zero. Magnetic current **M** in (4.4) is impressed (i.e. independent on field **E**) on the gap area S_a and is zero elsewhere on the remaining surface of the dipole S_{PEC}. The impressed incident field $\mathbf{E}^{inc}$ of **M** induces a current density **J** on the surface of PEC, which generates such scattered field $\mathbf{E}^{sca}$ that has tangential component negative of the tangential component of the incident field, i.e., $\hat{\mathbf{n}} \times \mathbf{E}^{inc} = - \hat{\mathbf{n}} \times \mathbf{E}^{sca}$ on the surface of the former air gap S_a. Outside the gap region and across the remaining part of PEC conductor, the tangential component of the scattered field $\mathbf{E}_t^{sca}$ vanishes because of the PEC material. Hence, the total electric field **E** is zero throughout the entire volume of the PEC material of the antenna including the volume of the former air gap.

The above equivalent field representation can be used to form the EFIE with respect

to the unknown surface current density $\mathbf{J}$. To that end, the tangential component of the total electric field $\mathbf{E}$ is forced to be zero on the boundary as

$$\hat{\mathbf{t}} \cdot \mathbf{E}^{inc}(\mathbf{r}) + i\omega\mu_0 \hat{\mathbf{t}} \cdot \int\limits_{S_{PEC}} \overline{\overline{G}}_{e0}(\mathbf{r}, \mathbf{r}') \cdot \mathbf{J}(\mathbf{r}')\, dS' = 0, \quad \mathbf{r} \in S_{PEC}, \tag{4.5}$$

where $\hat{\mathbf{t}}$ is the tangential vector to the boundary, and

$$\mathbf{E}^{inc}(\mathbf{r}) = \int\limits_{S_a} \overline{\overline{G}}_{m0}(\mathbf{r}, \mathbf{r}') \cdot \mathbf{M}(\mathbf{r}')\, dS'. \tag{4.6}$$

Note that $\mathbf{E}^{inc}$ produced by the impressed magnetic frill current $\mathbf{M}$ is non-zero everywhere in space. However, for convenience and simplicity it is typically approximated by the field of an infinite magnetic solenoid within the delta-gap region V_a and assumed to be zero everywhere else

$$\begin{aligned} &\mathbf{E}^{inc}(\mathbf{r}) \simeq \hat{\mathbf{n}}(\mathbf{r}_0) \times \mathbf{M}(\mathbf{r}_0), \quad \mathbf{r} \in V_a, \mathbf{r}_0 \in S_a \\ &\mathbf{E}^{inc}(\mathbf{r}) = 0, \quad \mathbf{r} \notin V_a. \end{aligned} \tag{4.7}$$

In EFIE (4.6) the solenoidal field approximation for $\mathbf{E}^{inc}$ is enforced on the surface S_{PEC} (note that surface S_a supporting $\mathbf{M}$ is included in S_{PEC}) as

$$\mathbf{E}^{inc} \simeq \begin{cases} \hat{\mathbf{n}} \times \mathbf{M}, & \mathbf{r} \in S_a, \\ \mathbf{0}, & \mathbf{r} \in S_{PEC} - S_a. \end{cases} \tag{4.8}$$

The "magnetic frill current" incident field approximation in (4.8) is exactly the same as that in the delta-gap model (4.14), provided the impressed magnetic current $\mathbf{M}$ is defined as $\hat{\mathbf{n}} \times \mathbf{M} = V\ \delta(p - p_0)\hat{\mathbf{p}}$.

4.4 Delta-Gap Source Model

The delta gap model approximates the physical excitation mechanism in dipole antenna driven by a voltage source applied at a small gap in the middle of it as shown in Fig. 4.5. Mathematical delta-gap source model assumes that the incident field exists only in the air gap between the antenna input terminals and is zero outside.

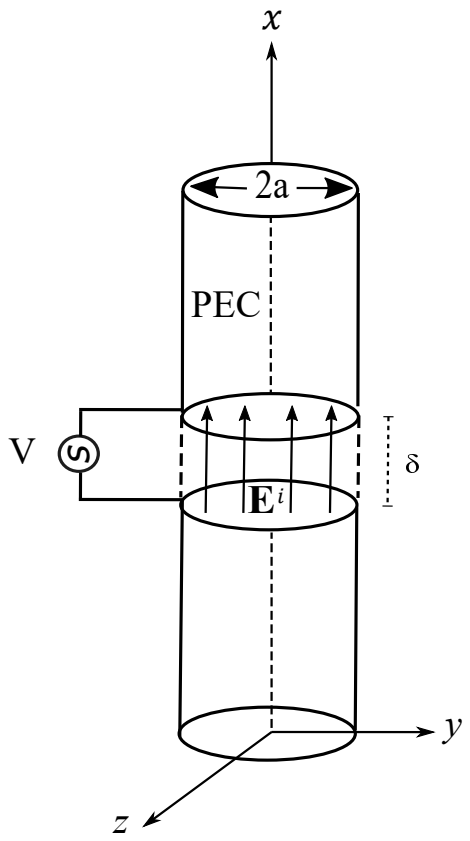

FIGURE 4.5: A physical model of delta-gap source.

In order to use the delta-gap source excitation in EFIE, an alternative model can be considered. Specifically, one can fill the air gap with PEC material making the dipole antenna a solid single-region PEC object Fig. 4.6. Then, one can impress an incident electric field at the boundary of the former air gap.

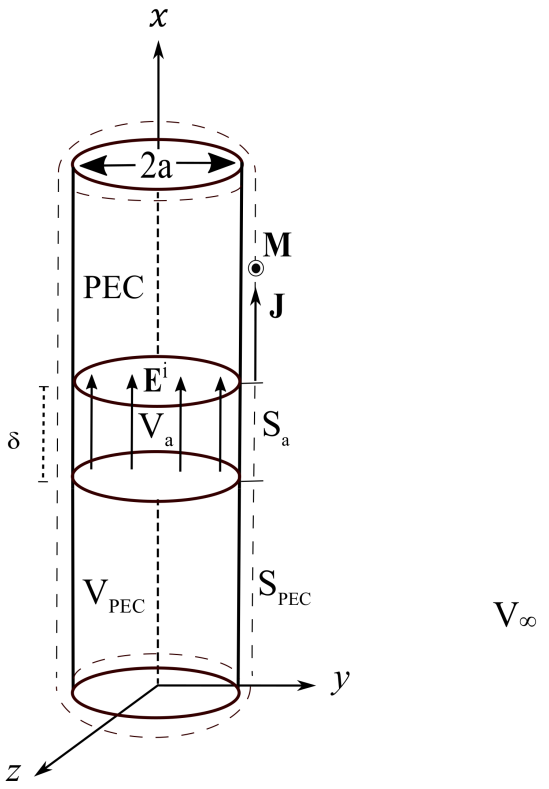

FIGURE 4.6: An equivalent problem of perfect electric conductor (PEC) used for delta-gap modeling with an incident field $\mathbf{E}^{inc}$ impressed in the volume V_a situated in the middle of the antenna structure volume V_{PEC} (V_{PEC} includes V_a). Surface S_{PEC} encloses volume of antenna V_{PEC} and includes surface S_a, S_a being the surface of the prior delta-gap region (gap is now filled with PEC).

Applying the exterior equivalence principle to the volume outside the dipole region V_{PEC}, we can express the total electric field outside the PEC region in terms of the equivalent electric and magnetic currents, as follows:

$$\mathbf{E}(\mathbf{r}) = \mathbf{E}^{inc}(\mathbf{r}) + i\omega\mu_0 \int\limits_{S_{PEC}} \overline{\overline{G}}_{e0}(\mathbf{r},\mathbf{r}') \cdot \mathbf{J}(\mathbf{r}')\, dS' + \int\limits_{S_{PEC}} \overline{\overline{G}}_{m0}(\mathbf{r},\mathbf{r}') \cdot \mathbf{M}(\mathbf{r}')\, dS',$$

$$\mathbf{r} \in V_\infty - V_{PEC}, \tag{4.9}$$

where

$$\begin{cases} \mathbf{J} = \hat{\mathbf{n}} \times \mathbf{H}, \\ \mathbf{M} = \mathbf{E} \times \hat{\mathbf{n}}. \end{cases} \tag{4.10}$$

and V_∞ specifies the entire space, while S_{PEC} encloses PEC volume V_{PEC}. The magnetic current $\mathbf{M}$ vanishes due to the fact that the tangential component of the total electric field on PEC surface is zero. The impressed electric field $\mathbf{E}^{inc}$ is assumed to be non-zero in the volume of the prior delta-gap region V_a and zero everywhere else in space $V_\infty - V_a$, i.e.

$$\begin{aligned} &\mathbf{E}^{inc}(\mathbf{r}) = \lim_{\Delta \to 0} \frac{V}{\Delta} \hat{\mathbf{p}} = V \ \delta(p - p_0)\hat{\mathbf{p}}, \quad \mathbf{r} \in V_a, \\ &\mathbf{E}^{inc}(\mathbf{r}) = 0, \quad \mathbf{r} \in V_\infty - V_a. \end{aligned} \tag{4.11}$$

The presence of the incident field $\mathbf{E}^{inc}$ induces a current density $\mathbf{J}$ on the surface of PEC, which generates scattered field $\mathbf{E}^{sca}$. The sum of scattered and incident fields produces the total electric field in the volume exterior to the volume of the antenna

$$\mathbf{E}(\mathbf{r}) = \mathbf{E}^{inc}(\mathbf{r}) + i\omega\mu_0 \int\limits_{S_{PEC}} \overline{\overline{G}}_{e0}(\mathbf{r}, \mathbf{r}') \cdot \mathbf{J}(\mathbf{r}') \ dS', \quad \mathbf{r} \in V_\infty - V_{PEC}. \tag{4.12}$$

The above equivalent field representation can be used to form the EFIE with respect to the unknown surface current density $\mathbf{J}$. To that end, the tangential component of the total electric field $\mathbf{E}$ is forced to be zero on the boundary S_{PEC} as

$$\hat{\mathbf{t}} \cdot \mathbf{E}^{inc}(\mathbf{r}) + i\omega\mu_0 \hat{\mathbf{t}} \cdot \int\limits_{S_{PEC}} \overline{\overline{G}}_{e0}(\mathbf{r}, \mathbf{r}') \cdot \mathbf{J}(\mathbf{r}') \ dS' = 0, \quad \mathbf{r} \in S_{PEC}, \tag{4.13}$$

where $\hat{\mathbf{t}}$ is the tangential vector to the boundary S_{PEC} and

$$\mathbf{E}^{inc}(\mathbf{r}) = \begin{cases} V \ \delta(p - p_0)\hat{\mathbf{p}}, & \mathbf{r} \in S_a, \\ \mathbf{0}, & \mathbf{r} \in S_{PEC} - S_a. \end{cases} \tag{4.14}$$

The current $\mathbf{J}$ is required to produce the tangential component of the scattered field that is negative of the incident field, i.e., $\hat{\mathbf{t}} \cdot \mathbf{E}^{inc} = - \hat{\mathbf{t}} \cdot \mathbf{E}^{sca}$ on the surface of the former air gap S_a and, hence, zero tangential component of the total electric field $\mathbf{E}$ everywhere on S_{PEC}. The condition $\hat{\mathbf{t}} \cdot \mathbf{E}(\mathbf{r}) = 0, \mathbf{r} \in \mathbf{S}_{PEC}$ in its turn enforces $\mathbf{E}(\mathbf{r}) = \mathbf{0}, \mathbf{r} \in V_{PEC}$ through the entire PEC volume of the antenna (including delta-gap volume V_a filled with PEC).

4.5 The MoM Discretization of EFIE with Delta-Gap Source Model

The MoM discretization of EFIE is achieved by edge-based basis functions, such as RWG which adapt to any arbitrary-shaped geometry. The electric-field integral equation for a PEC surface which satisfies the boundary conditions on S_{PEC} is given by

$$\mathbf{E}_t^{sca}\ (\mathbf{J}) = -\mathbf{E}_t^{inc}, \quad \mathbf{r} \in S_{PEC}. \tag{4.15}$$

The integral equation can be solved via MoM by discretizing the surface of the conductor with 2D mesh, consisting of M triangles. Let $\{\mathbf{f}_n\}_{n=1}^{N}$ be a set of N RWG basis functions defined on surface S_{PEC} in order to discretize the unknown surface current density. The RWG expansion of $\mathbf{J}$ is given by

$$\mathbf{J} = \sum_{n=1}^{N} I_n\ \mathbf{f}_n, \tag{4.16}$$

where I_n are unknown coefficients.

Substituting the RWG expansion of **J** (4.16) into EFIE formulation (4.15) yields

$$\sum_{n=1}^{N} I_n \ \mathbf{E}_t^{sca}(\mathbf{f}_n) = -\mathbf{E}_t^{inc}. \tag{4.17}$$

Galerkin's MoM method is subsequently applied to test the former expansion (4.17), where the testing functions $\mathbf{f}_m$ are defined to be equal to the basis functions $\mathbf{f}_n$ that is

$$\sum_{n=1}^{N} I_n \ \langle \mathbf{E}_t^{sca}(\mathbf{f}_n), \mathbf{f}_m \rangle = -\langle \mathbf{E}_t^{inc}, \ \mathbf{f}_m \rangle, \quad m = 1, 2, ..., N. \tag{4.18}$$

To simplify the numerical solution, it is convenient to reduce the gap to an infinitesimally small region. Thus, the impressed field in delta-gap can be viewed to be confined to a contour line ℓ on the conductor cross-section. A set of RWG basis functions is attached to contour line ℓ, and the common edges of those functions form a port. A linear system of equations with unknown coefficients $I_1, ..., I_n$ can be

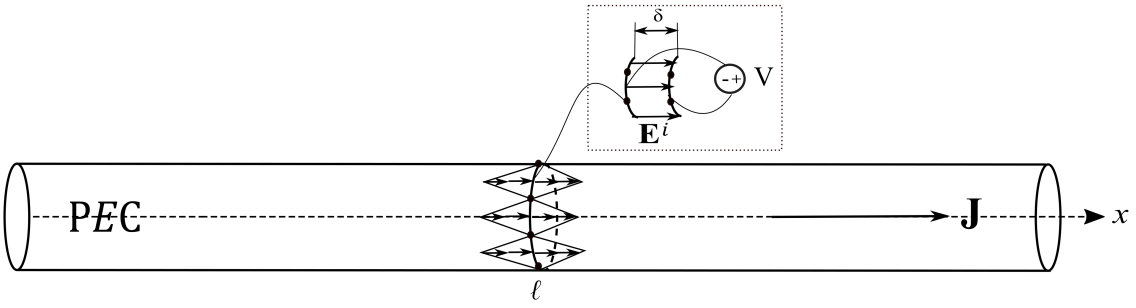

FIGURE 4.7: A perfectly conducting cylinder (PEC) with a gap implemented as line on the boundary of the conductor. The RWG basis functions attached to the line formed by the conductor cross-section contour ℓ. The impressed field $\mathbf{E}^{inc}$ is concentrated on the common edge of the RWG functions with the port line ℓ.

obtained from (4.18) as

$$\sum_{n=1}^{N} Z_{mn} \ I_n = V_m, \tag{4.19}$$

with

$$Z_{mn} = \langle \mathbf{E}_t^{sca}(\mathbf{f}_n), \mathbf{f}_m \rangle = \iint\limits_{S_m} \mathbf{E}_t^{sca}(\mathbf{f}_n) \cdot \mathbf{f}_m \; dS,$$

$$V_m = -\langle \mathbf{E}_t^{inc}, \mathbf{f}_m \rangle = -\iint\limits_{S_m} \mathbf{E}_t^{inc}(\mathbf{f}_n) \cdot \mathbf{f}_m \; dS,$$

where $\boldsymbol{Z}$ is the moment-matrix whose entries are the interactions between RWG basis functions and $\boldsymbol{I}$ is a coefficient-expansion vector of RWGs. $\boldsymbol{V}$ is the excitation vector. Due to the fact that the incident field is confined to a single common edge of an RWG basis function, $\boldsymbol{V}$ has as many non-zero entries as many RWG functions share the edge with the port line ℓ.

The vector of the unknown coefficients $\boldsymbol{I}$ is computed using the given excitation vector $\boldsymbol{V}$ and MoM matrix $\boldsymbol{Z}$ as $\boldsymbol{I} = \boldsymbol{Z}^{-1} \cdot \boldsymbol{V}$. Consequently, current density on surface of antenna $\mathbf{J}$ can be obtained by substituting coefficients I_n into expansion (4.16).

The input impedance Z_{in} of the dipole antenna is computed as the ratio between the applied voltage V at the input terminals of the antenna and the total current i through the port

$$Z_{in} = \frac{V}{i}, \tag{4.20}$$

with

$$i = \sum_{p=1}^{\mathcal{P}} I_{n(p)} \ell_{n(p)}, \tag{4.21}$$

where $\mathcal{P}$ is the number of the RWG functions sharing edge with the port line ℓ, $I_{n(p)}$ is the coefficients of nth RWG function attached to the port, $\ell_{n(p)}$ is the length of the edge of the nth RWG function sharing the edge with the port.

4.6 Delta-Gap Excitation Modeling for SVS-EFIE formulation

Recall the volume equivalence principle which is used to form the V-EFIE by equating the total electric field inside volume of an object to the sum of the incident electric field and the scattered electric field produced by the polarization current $\boldsymbol{j} = k_0^2(\epsilon_r - 1)\mathbf{E}$

$$\mathbf{E}(\mathbf{r}) = \mathbf{E}^{inc}(\mathbf{r}) + k_0^2(\epsilon_r - 1)\int_V \bar{\bar{G}}_{e0}(\mathbf{r}, \mathbf{r}') \cdot \mathbf{E}(\mathbf{r}')\, dV', \quad \mathbf{r} \in V. \tag{4.22}$$

The total field $\mathbf{E}$ can be represented as the superposition of the waves emanating from the object's boundary ∂V and weighted by the unknown surface current density $\boldsymbol{\mathcal{J}}$, that is

$$\mathbf{E}(\mathbf{r}) = -j\omega\mu_0 \int_{\partial V} \bar{\bar{G}}_{e\epsilon}(\mathbf{r}, \mathbf{r}') \cdot \boldsymbol{\mathcal{J}}(\mathbf{r}')\, dS', \quad \mathbf{r} \in \partial V. \tag{4.23}$$

The distribution of the electric field inside the object volume is governed by the current on the boundary, thus, the contribution to the field in V comes from the current $\boldsymbol{\mathcal{J}}$ on ∂V. For that reason, the field representation in (4.23) is constrained through enforcement of the volume EFIE on the boundary ∂V instead of being enforced through the entire volume V and only for the tangential component of the total field $\mathbf{E}$. This leads to the following equation

$$\hat{\mathbf{t}} \cdot \mathbf{E}(\mathbf{r}) - k_0^2(\epsilon_r - 1)\hat{\mathbf{t}} \cdot \int_V \bar{\bar{G}}_{e0}(\mathbf{r}, \mathbf{r}') \cdot \mathbf{E}(\mathbf{r}')\, dV' = \hat{\mathbf{t}} \cdot \mathbf{E}^{inc}(\mathbf{r}), \quad \mathbf{r} \in \partial V, \tag{4.24}$$

where $\hat{\mathbf{t}}$ is the tangential vector to the surface, and the total electric field $\mathbf{E}$ is given by (4.23).

The preceding integral representation constitutes SVS-EFIE with respect to the

unknown current density $\boldsymbol{\mathcal{J}}$ on the boundary. Similarly, the incident field is restricted to the boundary of the object. Thus, the delta-gap source model of EFIE derived in Section 4.4 can be extended to the SVS-EFIE. The MoM discretization of SVS-EFIE for plane wave or point source excitation was described in details in [27]. Handling of the excitation with the delta-gap port model in the MoM discretization of the SVS-EFIE formally is done in the same way as in the standard EFIE (see Section 4.5 for details). The MoM discretization of the SVS-EFIE yields a set of linear algebraic equations that is solved for coefficients of expansion of surface current $\boldsymbol{\mathcal{J}}$ over RWG functions. Thereafter, the obtained current is used to compute volume current of conductivity $\mathbf{j} = \sigma\mathbf{E}$ through the conductor material of the antenna. The net current through the delta-gap port is computed as the flux of the conductivity current through the cross-section of the port as

$$i = \int_S \mathbf{j} \cdot \hat{\mathbf{n}} \, dS, \tag{4.25}$$

where $\mathbf{j}$ is the conductivity current at the centroid of the tetrahedrons sharing one facet with triangles discretizing conductor cross-section at the port, $\hat{\mathbf{n}}$ is the normal to the plane of the port cross-section and opposite to the direction of the incident electric field in the delta-gap port definition, see Fig. 4.8. Particularly, the current is obtained at the centroid of tetrahedrons that share a face with the triangular meshes that discretize the plane.

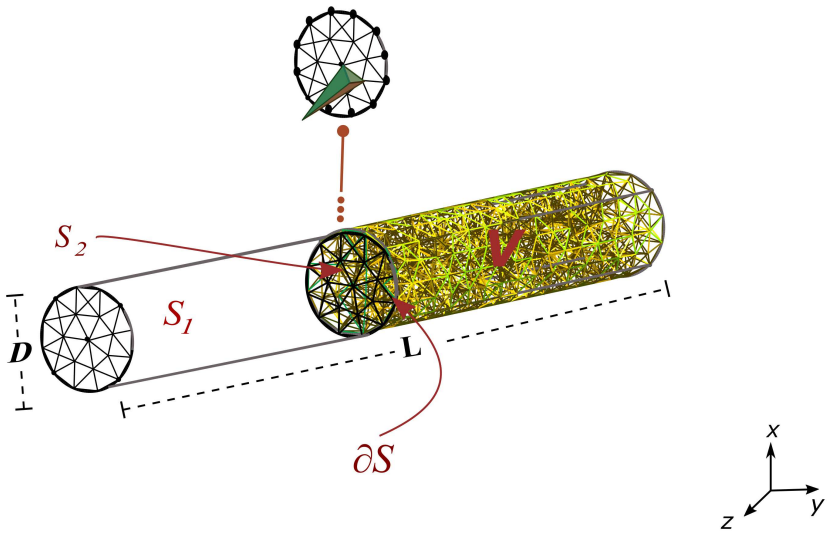

FIGURE 4.8: Dipole antenna of length L and diameter D with a surface port in the middle.

The input impedance Z_{in} of the dipole antenna is computed from the ratio between the applied voltage at the input terminals of the antenna and the total current through the port

$$Z_{in} = \frac{V}{i}. \tag{4.26}$$

To justify the use of conductivity current $\mathbf{j} = \sigma\mathbf{E}$ in the definition (4.25) of the net current at the port let's consider polarization current in a metal antenna. The imperfect conductor of the antenna (e.g. copper, steel, etc.) with finite conductivity σ has complex absolute permittivity

$$\epsilon(\boldsymbol{r}) = \epsilon_r(\boldsymbol{r})\varepsilon_0 = \varepsilon_r(\boldsymbol{r})\varepsilon_0 \left[1 + \frac{\sigma(\boldsymbol{r})}{i\omega\varepsilon_r(\boldsymbol{r})\varepsilon_0}\right]. \tag{4.27}$$

Since $\sigma(\boldsymbol{r})/i\omega\varepsilon_r(\boldsymbol{r})\varepsilon_0 \gg 1$, the polarization current $\boldsymbol{j}$

$$\boldsymbol{j}(\boldsymbol{r}) = i\omega[\epsilon(\boldsymbol{r}) - \varepsilon_0]\mathbf{E}(\boldsymbol{r}) = i\omega[\varepsilon_r(\boldsymbol{r})\varepsilon_0 + \frac{\sigma}{i\omega} - \varepsilon_0]\mathbf{E}(\boldsymbol{r}) \tag{4.28}$$

is close to the conductivity current $\mathbf{j}$ inside volume of good conductors, i.e., $\lim_{\sigma\to\infty} \boldsymbol{j} = \mathbf{j} = \sigma\mathbf{E}$, since

$$\boldsymbol{j}(\boldsymbol{r}) = [i\omega\varepsilon_r(\boldsymbol{r})\varepsilon_0 + \sigma - i\omega\varepsilon_0]\mathbf{E}(\boldsymbol{r}) = [i\omega\varepsilon_0(\varepsilon_r(\boldsymbol{r}) - 1) + \sigma]\mathbf{E}(\boldsymbol{r}) \sim \sigma\mathbf{E}(\boldsymbol{r}) = \mathbf{j}(\boldsymbol{r}). \tag{4.29}$$

Chapter 5

Implementation and Numerical Results

5.1 SVS-EFIE Solution for Imperfectly Conducting Objects

The SVS-EFIE implementation was extended to scattering problems on 3D well-conducting objects in [16]. This extension takes advantage of sparsity added to the MoM discretization matrices of SVS-EFIE when the skin-effect is well developed. Under the conditions of the strong skin-effect the volumetric current density is localized near the surface turning SVS-EFIE into a surface-like SSIE but with a fewer integral operator products. This yields a reduction in computational steps and memory requirements. Here we reproduced these results by testing the SVS-EFIE solution against analytic Mie series solution for the scattering problem on metallic sphere in the regimes of weak, intermediate, and strong skin effects. The numerical solution was observed to be robust and error controllable.

Specifically, let's consider a lead sphere with radius equal to 5 µm and conductivity $\sigma = 4.5 \cdot 10^6$ S/m. The solution of the following scattering problem is first obtained

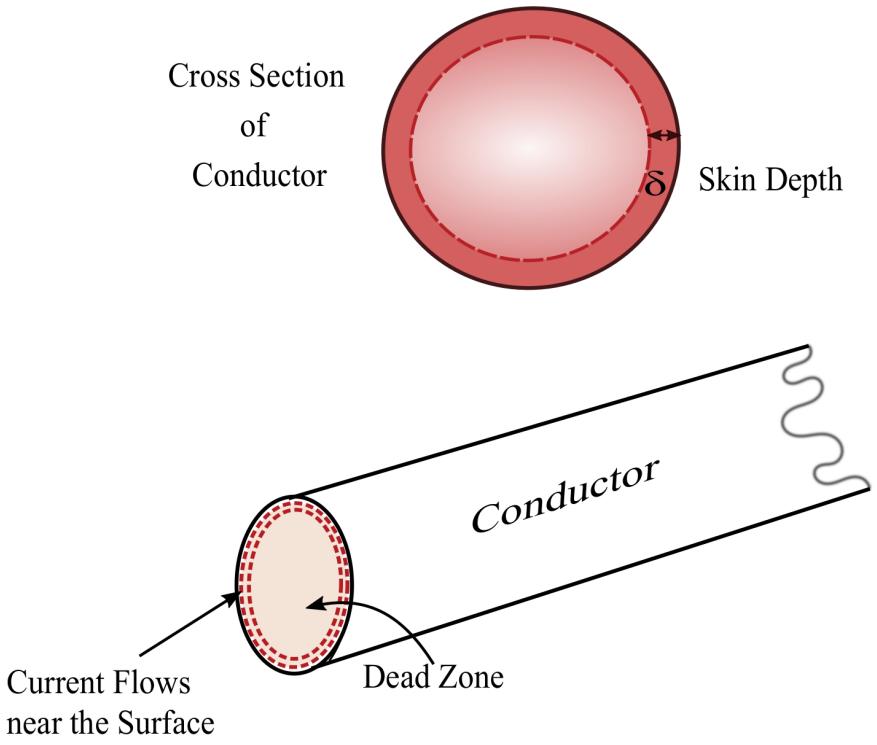

FIGURE 5.1: The Skin-depth effect on the distribution of current flow in a conductor under high-frequency condition.

using MoM discretization of the SVS-EFIE. Next, the comparison is performed against Mie series solution at following frequencies: 1 GHz, 50 GHz and 100 GHz with skin depth about 7.5 µm and 1.1 µm, respectively. The skin depth becomes smaller as frequency increases. The solution of SVS-EFIE discretized using MoM, however, provides an accurate solution with an average relative error in the range of 1-2%. The set-up parameters of the simulations are presented in Tables 5.1 and 5.3. The total electric field that is generated inside the volume of the sphere at different frequencies is illustrated in Figs. 5.2 and 5.4

TABLE 5.1: Discretization Parameters at $f = 1$ GHz.

Frequency 1 GHz	
No. of 2-D Elements	760
No. of 3-D Elements	4,507
No. of RWG Basis Functions	1,140
Average relative Error: Mie Series vs. SVS-EFIE 1.2%.	

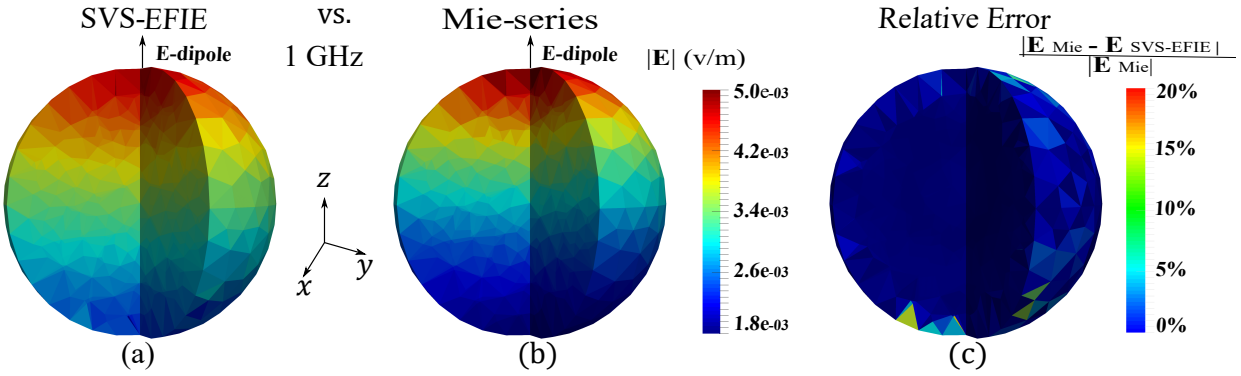

FIGURE 5.2: Magnitude of the total electric field in lead (Pb) sphere generated by a z-directed electric dipole situated at $x' = 0$ m, $y' = 0$ m, $z' = 0.00003$ m obtained by (a) SVS-EFIE and (b) Mie Series at 1 GHz. The relative error distribution with respect to the analytical solution is shown in (c).

TABLE 5.2: Discretization Parameters at $f = 50$ GHz.

Frequency 50 GHz	
No. of 2-D Elements	3,762
No. of 3-D Elements	52,843
No. of RWG Basis Functions	5,643
Average relative Error: Mie Series vs. SVS-EFIE 1.0%.	

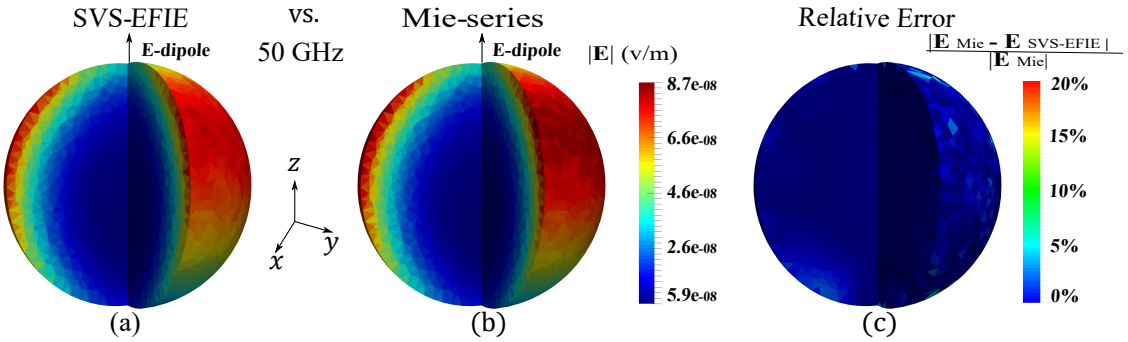

FIGURE 5.3: Magnitude of the total electric field in lead (Pb) sphere generated by a z-directed electric dipole situated at $x' = 0$ m, $y' = 0$ m, $z' = 0.00003$ m obtained by (a) SVS-EFIE and (b) Mie Series at 50 GHz. The relative error distribution with respect to the analytical solution is shown in (c).

TABLE 5.3: Discretization Parameters at $f = 100$ GHz.

Frequency 100 GHz	
No. of 2-D Elements	6,206
No. of 3-D Elements	106,441
No. of RWG Basis Functions	9,309
Average relative Error: Mie Series vs. SVS-EFIE 0.7%.	

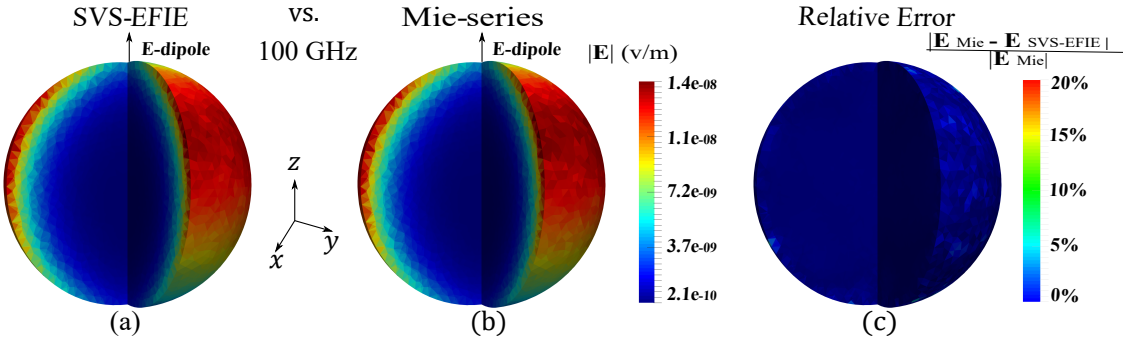

FIGURE 5.4: Magnitude of the total electric field in lead (Pb) sphere generated by a z-directed electric dipole situated at $x' = 0$ m, $y' = 0$ m, $z' = 0.00003$ m obtained by (a) SVS-EFIE and (b) Mie Series at 100 GHz. The relative error distribution with respect to the analytical solution is shown in (c).

The preceding results illustrate the relationship between the skin depth and the frequency. The skin depth is dependent on the frequency and is inversely proportional to the square root of it. The presence of strong skin-effect as the current starts flowing in a thin region near the surface of the conductor allows SVS-EFIE to obtain accurate solution provided at least two samples per skin-depth are maintained in the volumetric mesh. The SVS-EFIE solutions under the conditions of strong, intermediate and weak skin-effects in the radiation problem of the electric dipole near lead sphere at $f=$ 100 GHz, $f=$ 50 GHz and $f=$ 1 GHz has average relative error about 0.7%, 1.0% and 1.2%, respectively.

5.2 Solution of SVS-EFIE with Delta-Gap Source Model

The proposed port excitation model in the SVS-EFIE formulation is used to solve problem of dipole antenna radiation and its characterization in terms of the input impedance. The delta-gap source model in SVS-EFIE as well as its MoM discretization (developed prior to this work) are implemented using C++ programming language. The simulations were performed on the advanced compute clusters Grex and Cedar at the WestGrid consortium, which is a part of Compute Canada national network of high-performance computing facilities. The data analysis and visualizations were performed by Kitware's software ParaView [49].

In this work, a solution of dipole antenna radiation problem is obtained via MoM discretization of SVS-EFIE augmented with the proposed port excitation model. A dipole antenna made of lead rod and radiating in free space with frequency range $f \in [33.2, 133]$ THz, is considered. The length of the dipole is set to be $L = 2.5\,\mu$m and it is fed by a voltage gap $V = 1$ V in its center $(L/2)$. The preceding parameters were selected according to the measurements in [5, 44], where physical and

electrical sizes are maintained at particular ratios to determine the behavior of the input impedance at resonance condition. The simulations were accomplished for different cases with respect to the length-to-diameter ratio L/D. In each case of the simulation, the physical length L and the length-to-diameter ratio L/D are held constant, while the wavelength λ_0 is varying in order to obtain different antenna length-to-wavelength ratios L/λ_0.

In the first case, L/D is set to be equal to 10, while the length of the dipole is $L = 2.5\,\mu\text{m}$ and the diameter is $D = 250\,\text{nm}$. The simulation was carried out for the following electrical antenna lengths expressed in degrees ($\frac{180^\circ}{\pi}\frac{L}{\lambda_0}$): 50°, 75°, 100°, 125°, and 150°. The antenna was operated over the band of frequencies $f \in [33.2, 99.5]$ THz and the density of the mesh was specified to be 2 elements per skin depth at each frequency. The mesh density grows along with the frequency to capture the volumetric current behavior according to the skin-effect.
The total electric field in the lead cylindrical dipole generated by proposed δ-gap port at different frequencies is depicted in Fig. 5.5. The input impedance was obtained by SVS-EFIE solver and compared against EFIE augmented with the Leontovich surface impedance operator as well as EFIE solution for PEC antenna as illustrated in Fig. 5.6 and Fig. 5.7. The parameters of simulation and the input impedance values are given in Table 5.4.

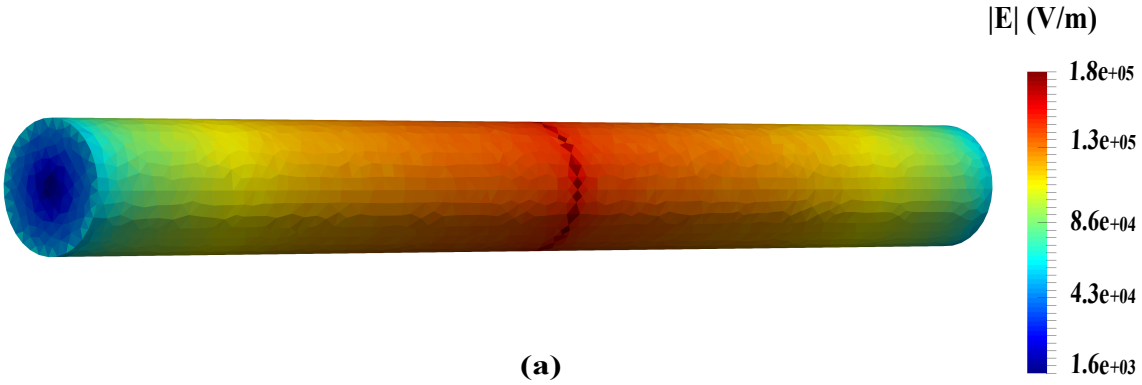
|E| (V/m)
1.8e+05
1.3e+05
8.6e+04
4.3e+04
1.6e+03

(a)

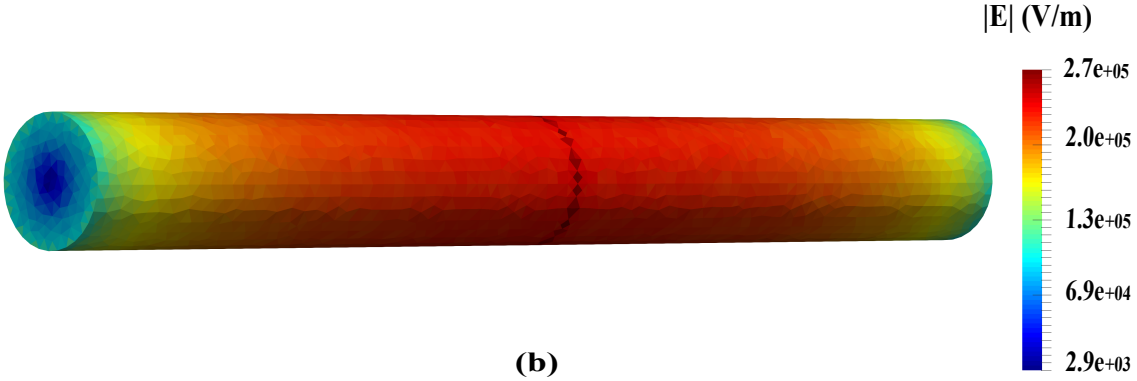
|E| (V/m)
2.7e+05
2.0e+05
1.3e+05
6.9e+04
2.9e+03

(b)

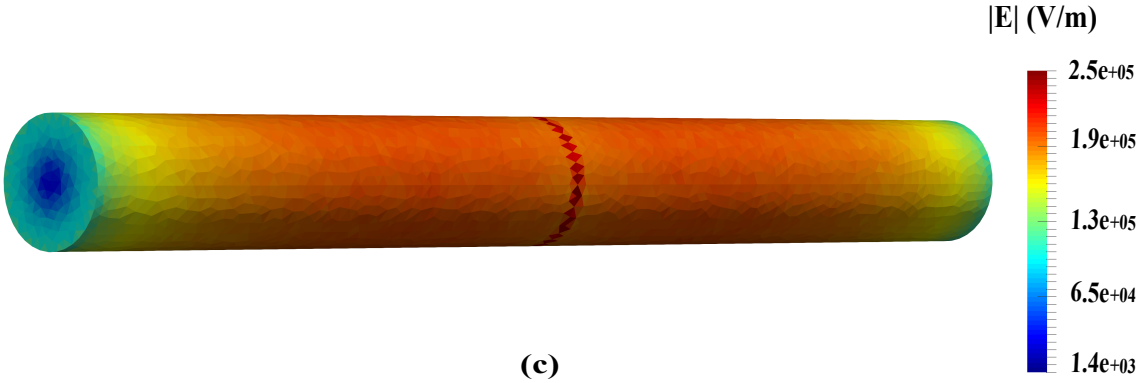
|E| (V/m)
2.5e+05
1.9e+05
1.3e+05
6.5e+04
1.4e+03

(c)

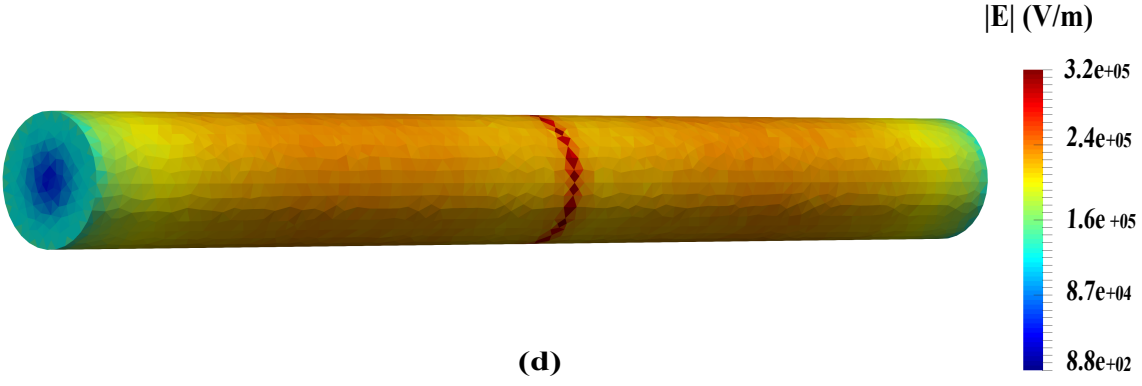
|E| (V/m)
3.2e+05
2.4e+05
1.6e +05
8.7e+04
8.8e+02

(d)

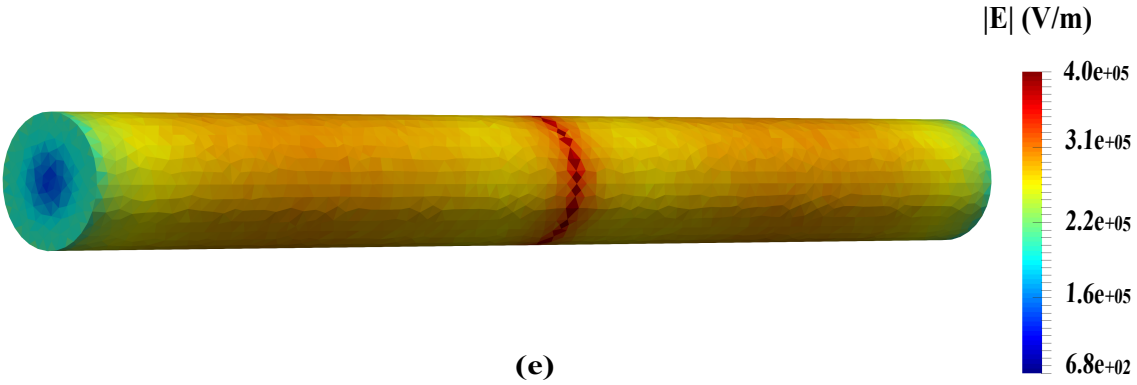

FIGURE 5.5: The total electric field in the lead cylindrical dipole generated by δ-gap port at different frequencies with $L/D = 10$ for the following electrical lengths: (a) 50°, (b) 75°,(c) 100°, (d) 125°, (e) 150°.

TABLE 5.4: Parameters of SVS-EFIE simulations for the dipole antenna input impedance computations with $L = 2.5\,\mu m$ and $D = 0.25\,\mu m$ (L/D=10).

L/λ	Frequency	Skin Depth	Impedance
50°	33.2 THz	40.97 nm	13.18 - 89.31i
75°	44.9 THz	35.23 nm	60.76 - 34.24i
100°	66.6 THz	28.92 nm	77.43 - 96.50i
125°	82.7 THz	25.96 nm	30.75 - 90.44i
150°	99.5 THz	23.67 nm	15.25 - 70.61i

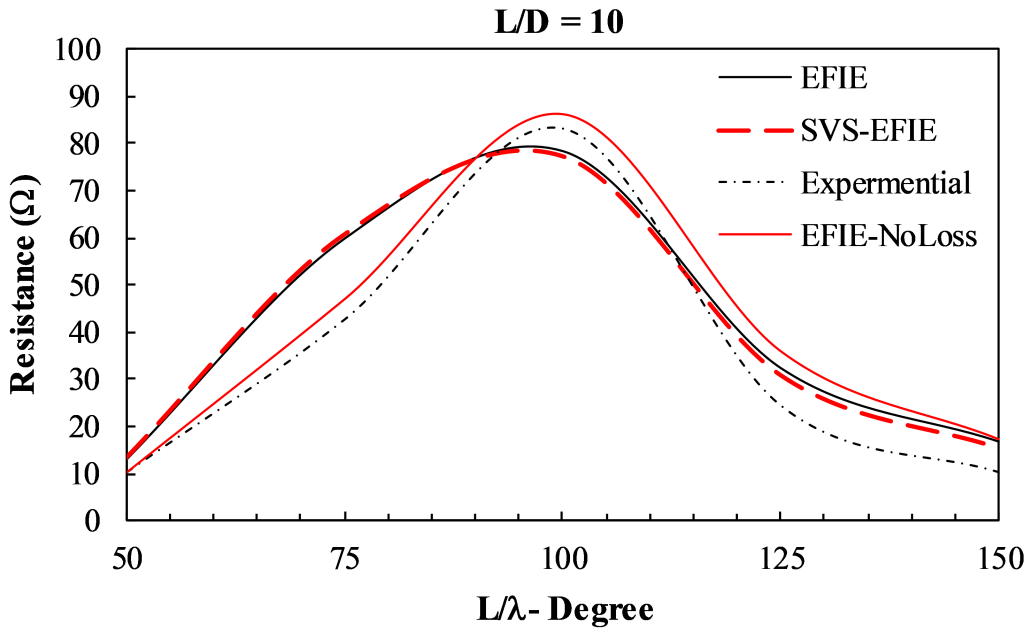

FIGURE 5.6: Dipole antenna input resistance with $L/D = 10$ from SVS-EFIE, EFIE without loss operator, EFIE with Leontovich surface impedance, and measurements [45].

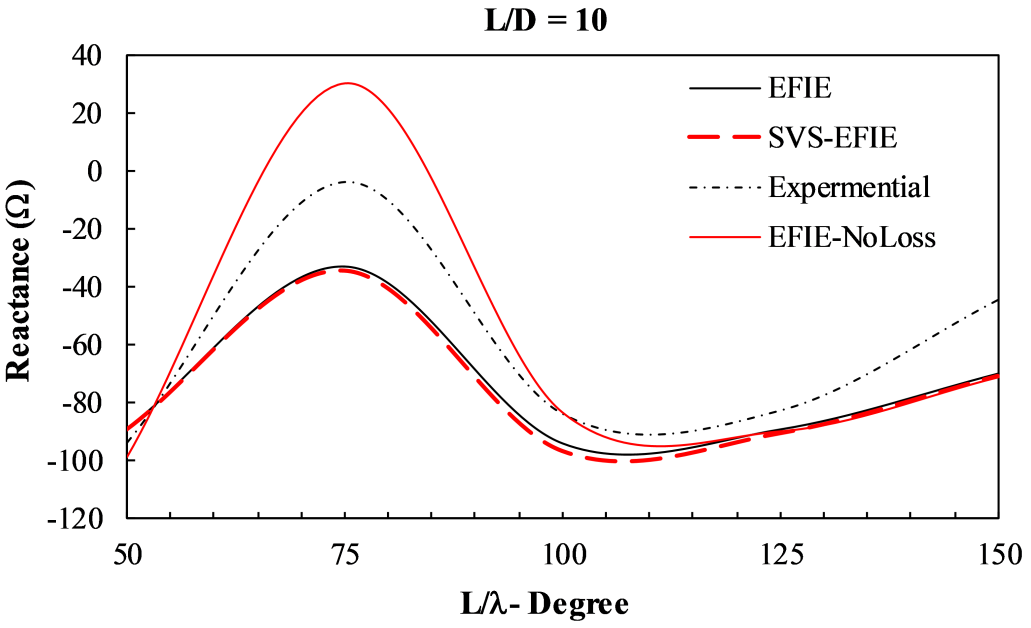

FIGURE 5.7: Dipole antenna input reactance with $L/D = 10$ from SVS-EFIE, EFIE without loss operator, EFIE with Leontovich surface impedance operator, and measurements [45].

The second test was performed for antenna with $L/D = 20$, where the length is $L = 2.5\,\mu\text{m}$ and the diameter is $D = 125\,\text{nm}$. The simulations were carried out for the following electrical lengths of the anteannae: 50°, 75°, 100°, 125° and 150° in the range of frequencies $f \in [33.2, 99.5]$ THz. The characteristic length of the volumetric and surface meshes was specified to be 0.5 skin depth.

The total electric field in the lead cylindrical dipole generated by surface port at different frequencies is depicted in Fig. 5.8. The input impedance was obtained by the proposed δ-gap driven SVS-EFIE formulation and tested against EFIE augmented with Leontovich surface impedance operator as well as EFIE solution for lossless antenna as illustrated in Fig. 5.9 and Fig. 5.10. The parameters of simulation and the input impedance values are presented in Table 5.5.

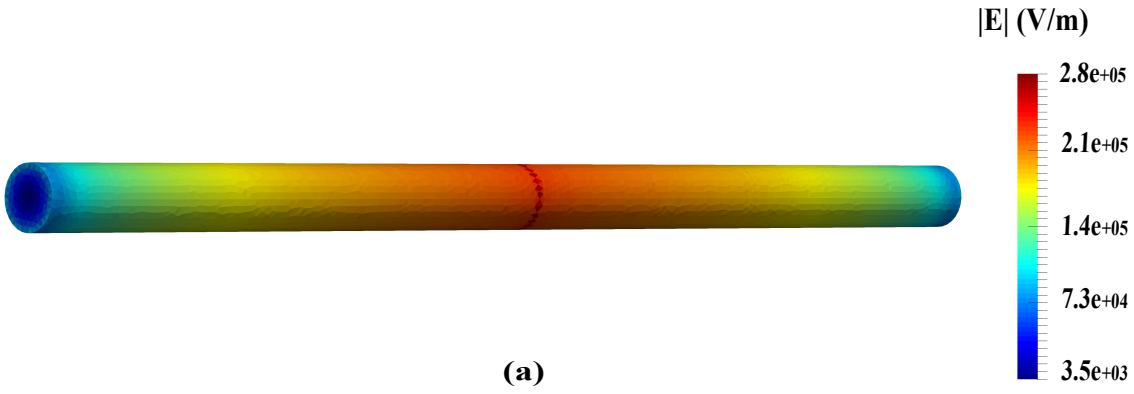
|E| (V/m)
2.8e+05
2.1e+05
1.4e+05
7.3e+04
3.5e+03

(a)

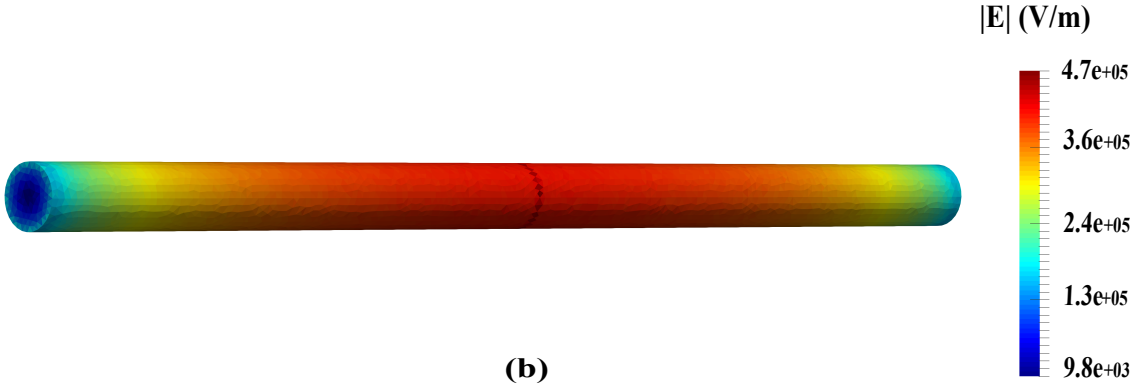
|E| (V/m)
4.7e+05
3.6e+05
2.4e+05
1.3e+05
9.8e+03

(b)

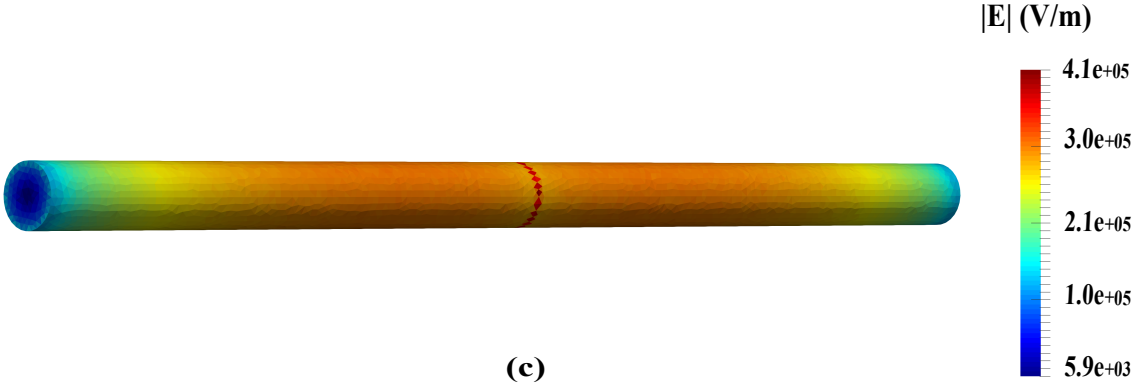
|E| (V/m)
4.1e+05
3.0e+05
2.1e+05
1.0e+05
5.9e+03

(c)

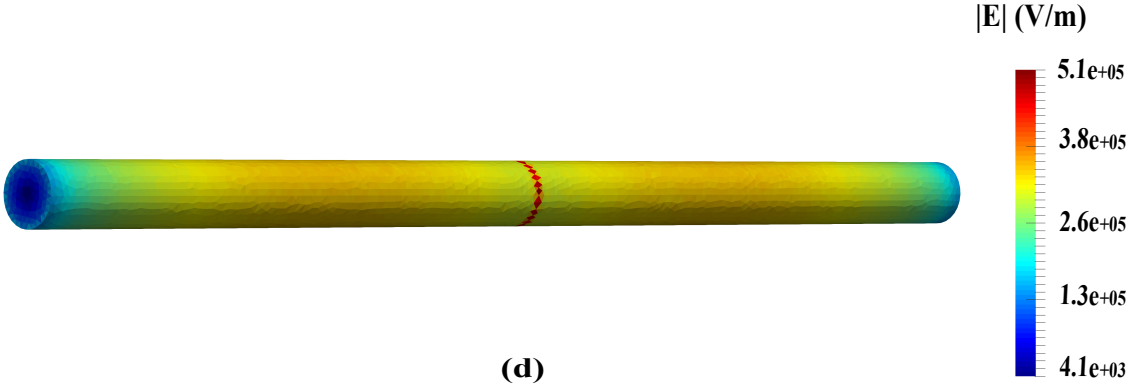
|E| (V/m)
5.1e+05
3.8e+05
2.6e+05
1.3e+05
4.1e+03

(d)

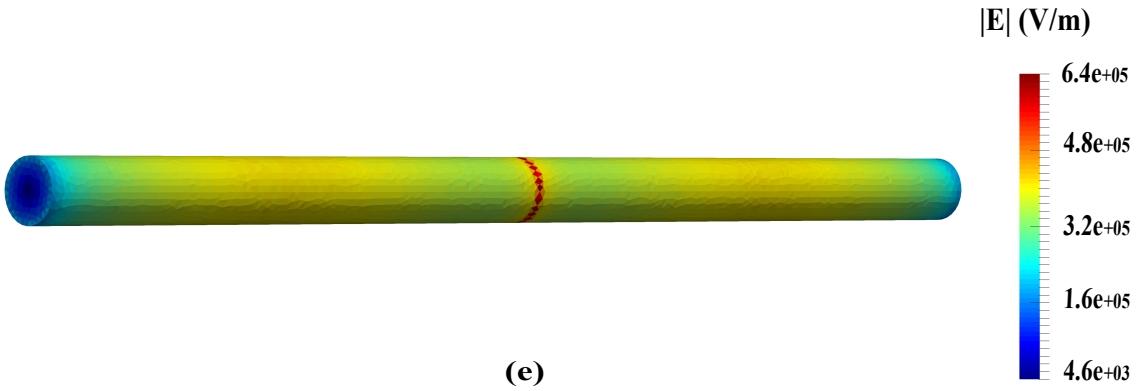

FIGURE 5.8: The total electric field in the lead cylindrical dipole generated by surface port at different frequencies with $L/D = 20$ for the following antenna length: (a) 50°, (b) 75°,(c) 100°, (d) 125°, (e) 150°.

.

TABLE 5.5: Parameters of SVS-EFIE Simulation for input impedance extraction of a dipole antenna with $L = 2.5\,\mu m$ and $D = 0.125\,\mu m$ (L/D=20).

L/λ	Frequency	Skin Depth	Impedance
50°	33.2 THz	40.97 nm	22.11 - 141.41i
75°	44.9 THz	35.23 nm	76.59 - 36.05i
100°	66.6 THz	28.92 nm	199.25 - 97.58i
125°	82.7 THz	25.96 nm	97.50 - 172.46i
150°	99.5 THz	23.67 nm	43.08 - 136.66i

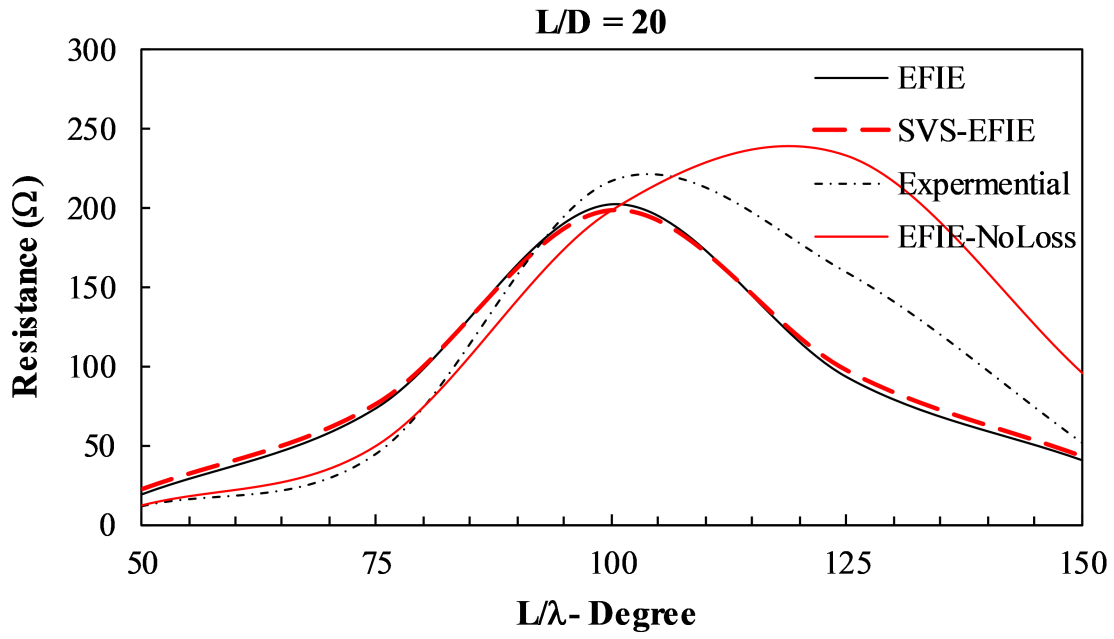

FIGURE 5.9: Input resistance of dipole antenna with L/D =20 from SVS-EFIE, EFIE without loss operator, EFIE with Leontovich surface impedance, and measurements. [45]

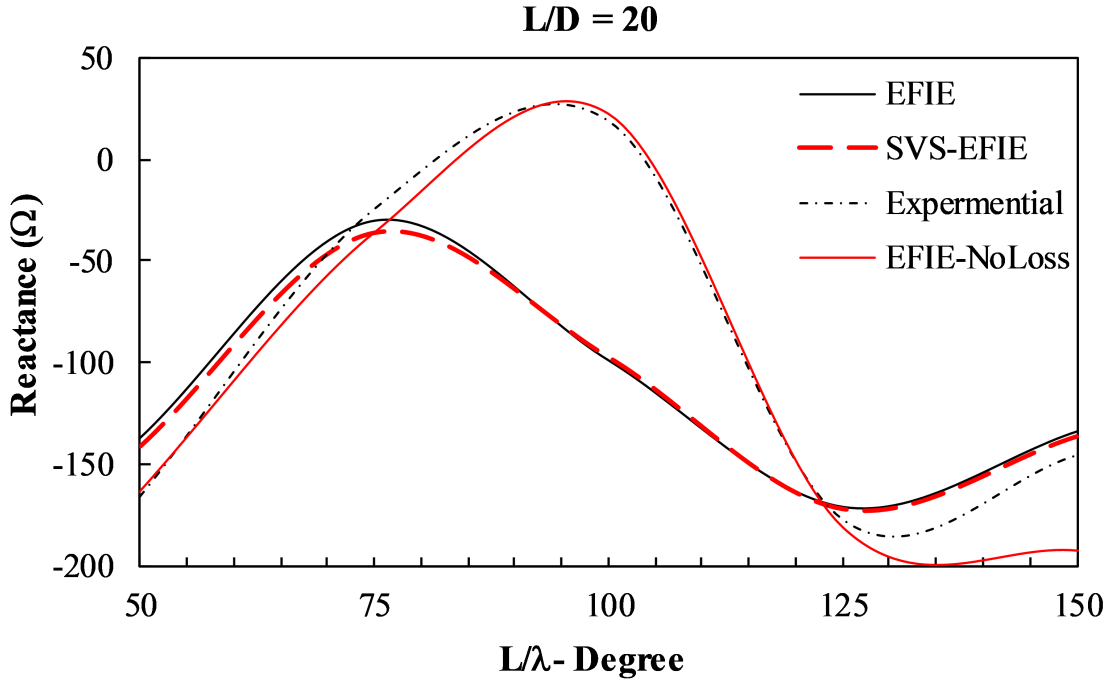

FIGURE 5.10: Input reactance of the dipole antenna with $L/D = 20$ from SVS-EFIE, EFIE without loss operator, EFIE with Leontovich surface impedance, and measurements. [45]

The last test was conducted for the case of dipole antenna with ($L/D = 40$), where the length is $L = 2.5\,\mu\text{m}$ and the diameter is $D = 62.5\,\text{nm}$. The simulation was carried out for the following antenna length: 50°, 75°, 100°, 125°, 150°, 175° and 200°. The antenna was operated over the band of frequencies $f \in [33.2, 133]$ THz and the characteristic size of the meshes was specified to be half the skin depth.
The total electric field in the lead cylindrical dipole generated by δ-gap port at different frequencies is depicted in Fig. 5.11. The total electric field at the cross-section is shown in Fig. 5.12 where it demonstrates the penetration of the current through the conductor cross-section as the skin depth is large compared with the radius of the wire. The input impedance was obtained by the proposed δ-gap driven SVS-EFIE formulation and tested against EFIE augmented with Leontovich surface impedance operator as well as EFIE solution for lossless antenna as illustrated in Fig. 5.13 and Fig. 5.14. The parameters of simulations and the input impedance values are presented in Table 5.5.

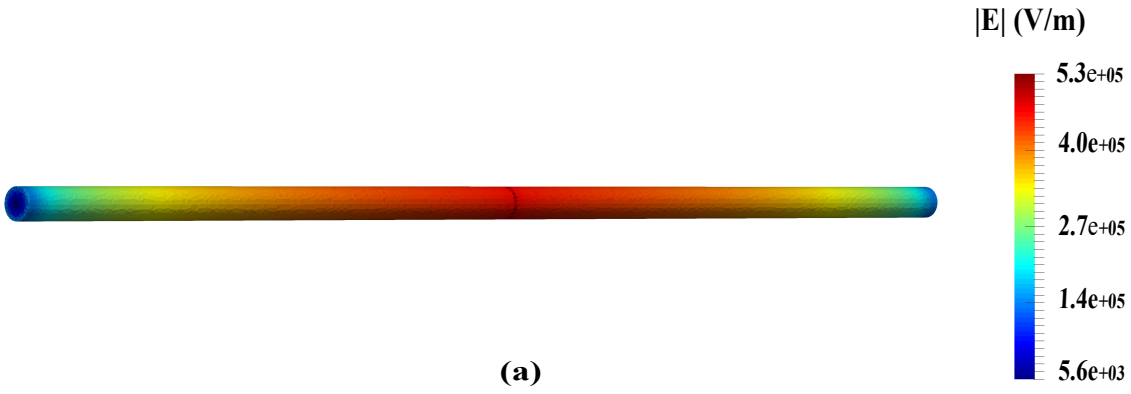
|E| (V/m)
5.3e+05
4.0e+05
2.7e+05
1.4e+05
5.6e+03

(a)

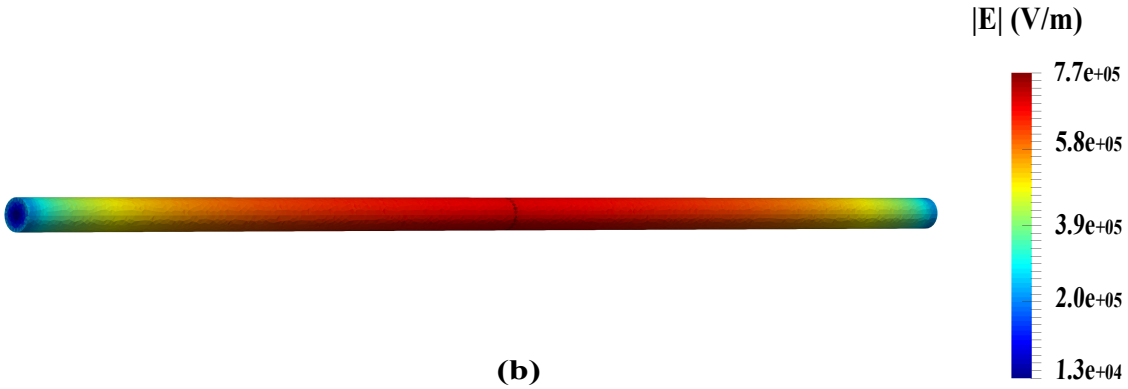
|E| (V/m)
7.7e+05
5.8e+05
3.9e+05
2.0e+05
1.3e+04

(b)

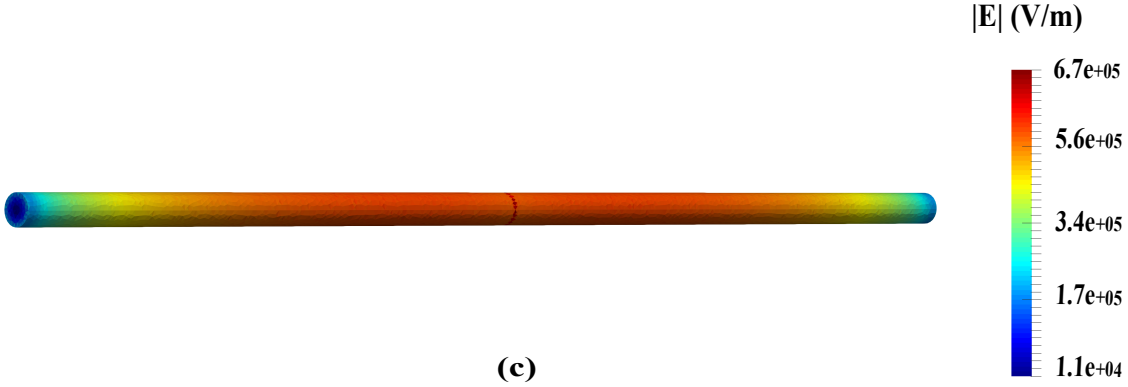
|E| (V/m)
6.7e+05
5.6e+05
3.4e+05
1.7e+05
1.1e+04

(c)

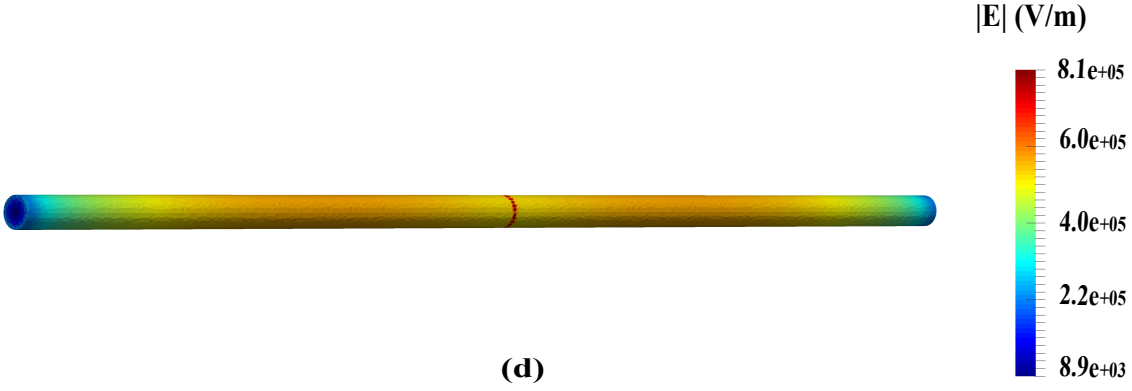
|E| (V/m)
8.1e+05
6.0e+05
4.0e+05
2.2e+05
8.9e+03

(d)

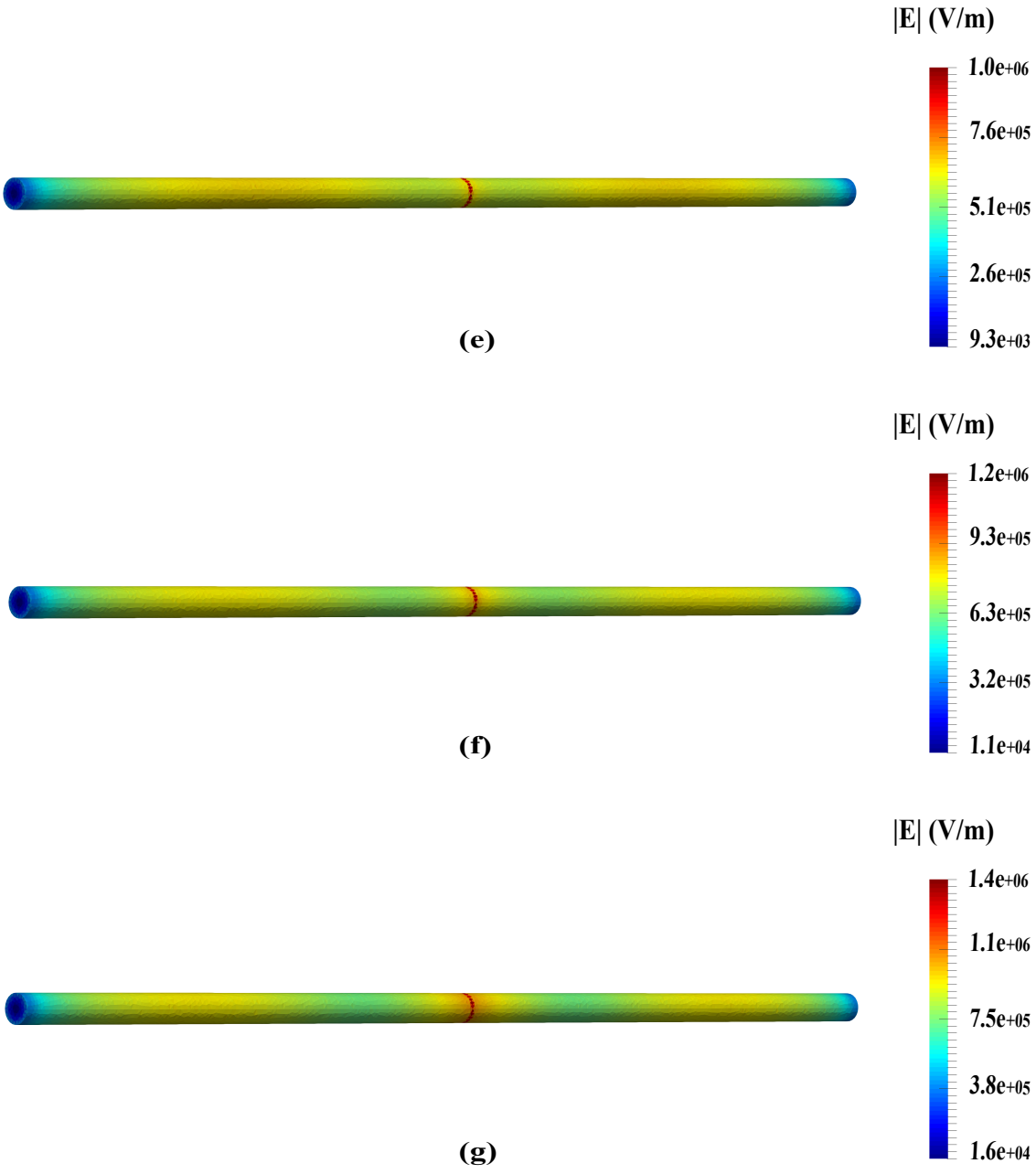

FIGURE 5.11: The total electric field in the lead cylindrical dipole generated by surface port at different frequencies with $L/D = 40$ for the following antenna length: (a) 50°, (b) 75°,(c) 100°, (d) 125°, (e) 150°, (f) 175°, (g) 200 °.

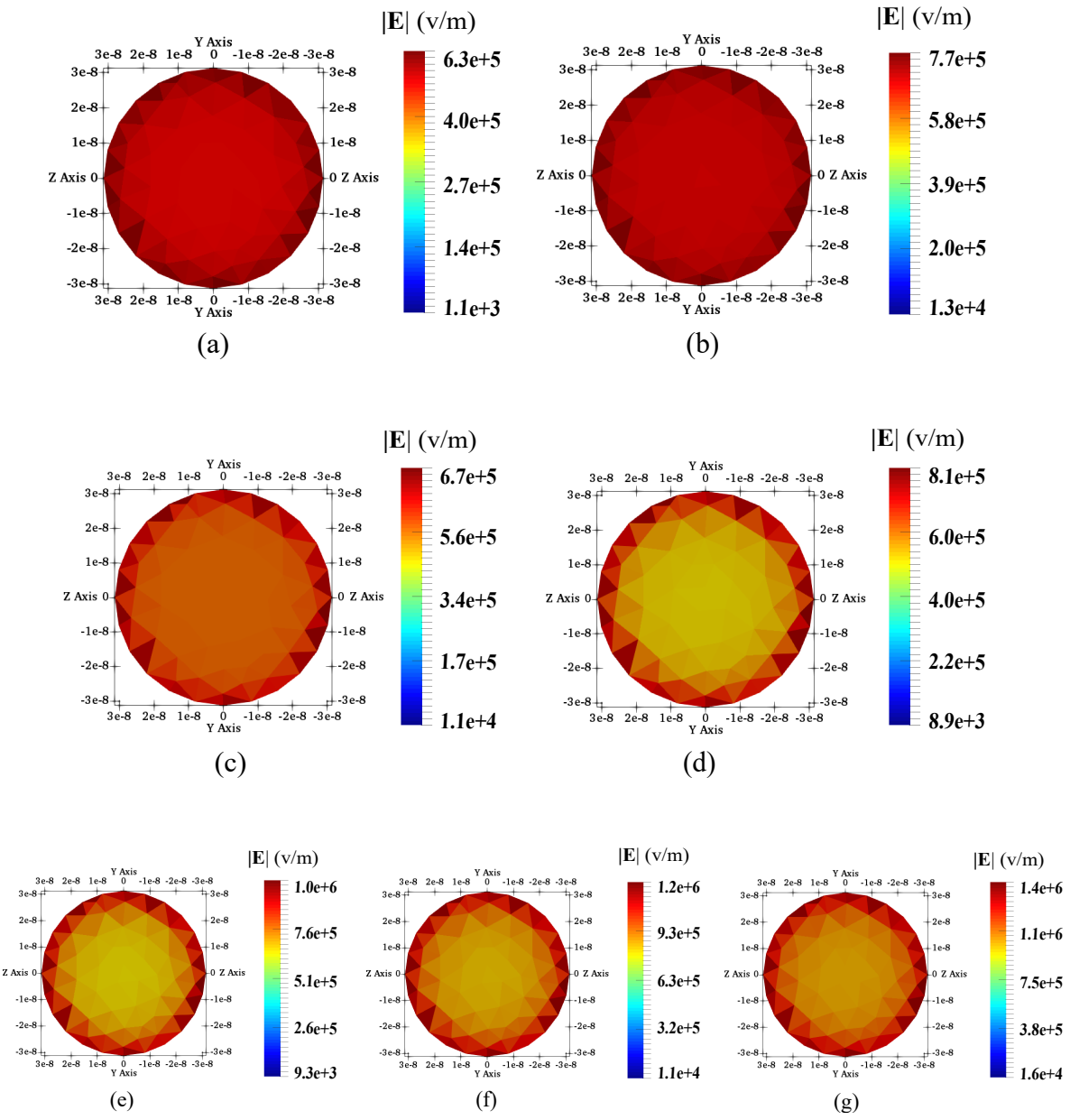

FIGURE 5.12: The current distribution at the cross-section of the dipole antenna with $L/D = 40$ for the following antennae electrical lengths (expressed in degrees): (a) 50°, (b) 75°,(c) 100°, (d) 125°, (e) 150°, (f) 175°, (g) 200 °.

TABLE 5.6: Parameters of SVS-EFIE simulations for input impedance extraction of a dipole antenna with $L = 2.5\,\mu m$ and $D = 62.5\,nm$ (L/D=40).

L/λ	Frequency	Skin Depth	Impedance
50°	33.2 THz	40.97 nm	57.71 - 210.36i
75°	44.9 THz	35.23 nm	122.47 - 73.02i
100°	66.6 THz	28.92 nm	270.52 - 84.07i
125°	82.7 THz	25.96 nm	220 - 241.82i
150°	99.5 THz	23.67 nm	103.78 - 225.52i
175°	117 THz	21.82 nm	58.99 - 172.86i
200°	133 THz	20.47 nm	47.71 - 130.81i

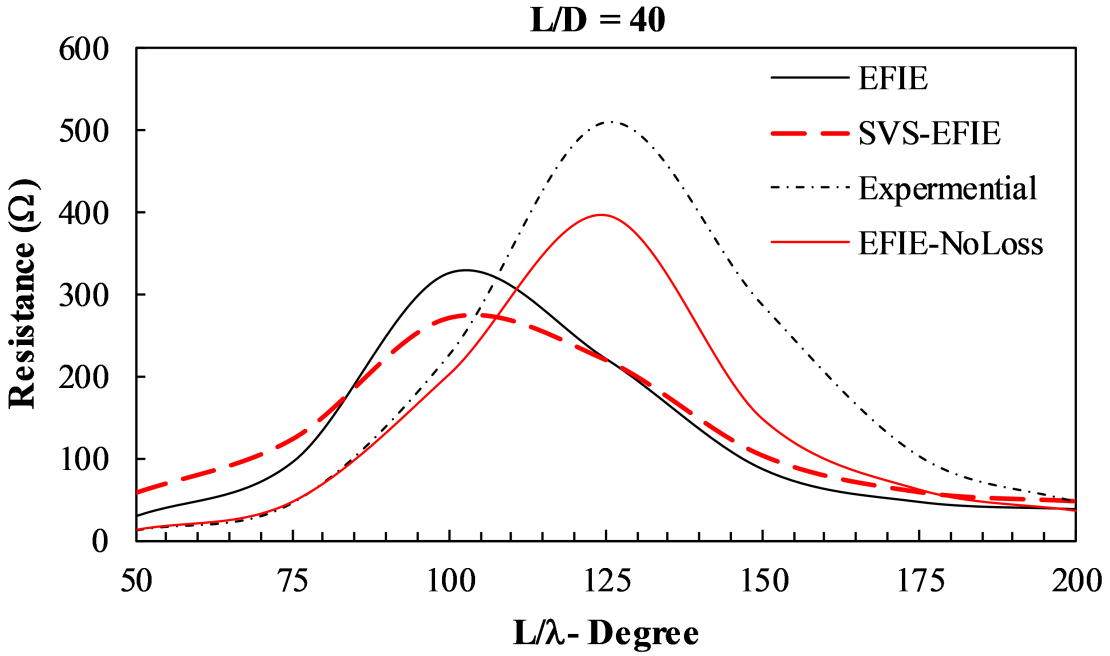

FIGURE 5.13: Input resistance the of dipole antenna with $L/D = 40$ from SVS-EFIE, EFIE without loss operator, EFIE with Leontovich surface impedance, and measurements. [45]

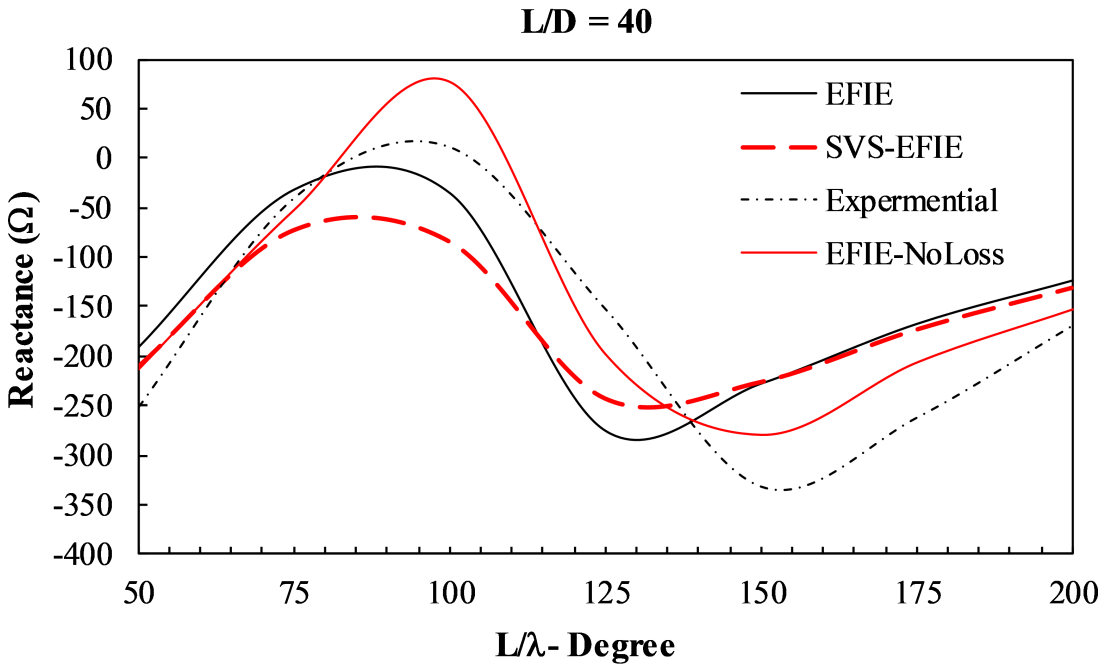

FIGURE 5.14: Input reactance of the dipole antenna with $L/D = 40$ from SVS-EFIE, EFIE without loss operator, EFIE with Leontovich surface impedance, and measurements. [45]

In the last case with $L/D = 40$ a small deviation can be noticed between the two numerical solutions due to the reduction in the radius size of the cylindrical wire. As the diameter of the wire is reduced, the ratio of the wire radius r_0 to the skin depth δ becomes smaller. Implementation in surface EFIE of the surface impedance for circular wire defined by the Bessel function [41] is expected to provide a better approximation for the current distribution in antenna with small (r_0/δ) ratios and yield smaller error in the value of the extracted input impedance. Such modification of the surface EFIE for obtaining accurate reference solutions at weak skin-effect regimes will be considered in the future work. We would like to note here also that 2D magneto-quasi-static solution of SVS-EFIE for circular wire has been tested against the analytic solution in [46].

As can be seen from the demonstrated results, the numerical impedance calculations using SVS-EFIE with proposed δ-gap excitation model match well the EFIE results when it is augmented with Leontovich surface impedance term under conditions of

the strong skin-effect. This serves as a proof of concept for the SVS-EFIE use in such important practical applications as antenna analysis, interconnect characterization, design of microwave components, and others.

5.3 Convergence Study of SVS-EFIE Results

An investigation on the convergence in MoM solution of the SVS-EFIE augmented with δ-gap port model was performed to ensure its robustness and insensitivity to the mesh density. The numerical results computed by SVS-EFIE through MoM discretization is based on an approximation of the computational domain by finite volume and surface element on a given geometry and field behaviour within each element. Hence, mesh density plays an important role in generating accurate results, with finer meshes generally providing more accurate solutions.

The following convergence study was performed via progressive mesh refinements and monitoring the results. Different mesh densities were considered in the SVS-EFIE simulations coarse, medium, fine, and extra-fine with 1.5, 2.0, 2.5, and 3.0 samples per skin-depth, respectively. The tests were performed for a dipole antenna where the geometry of the antenna, the material properties and the operation frequency were fixed for all levels of the mesh density.

In the simulations the antenna was excited by the proposed δ-gap port in the middle of the structure with length $L = 2.5\,\mu\text{m}$ and diameter $D = 125\,\text{nm}$. The length-to-diameter ratio was set to be $L/D = 20$. The material of the antenna structure was lead with $\sigma = 4.5 \cdot 10^6$ S/m. The antenna was operated at $f = 73.3$ THz. The MoM discretization of the SVS-EFIE is performed by using different number of samples per skin depth for the purpose of obtaining more accurate solutions in the process of mesh refinements. The size of the mesh was varied from $3,000$ triangles and $11,000$ tetrahedrons for discretization with one sample per skin depth to $15,000$ triangles and $125,000$ tetrahedrons for discretization with three samples per skin-depth. The

distribution of the current along the x axis of the dipole antenna is illustrated in Fig. 5.15 to display the steadiness of the SVS-EFIE solution. The current distributions at the port of the dipole for the coarse, medium, fine and extra-fine meshes are demonstrated in Fig. 5.16. The input impedance of the dipole antenna was extracted for the different sizes of the mesh and shown in Table 5.7.

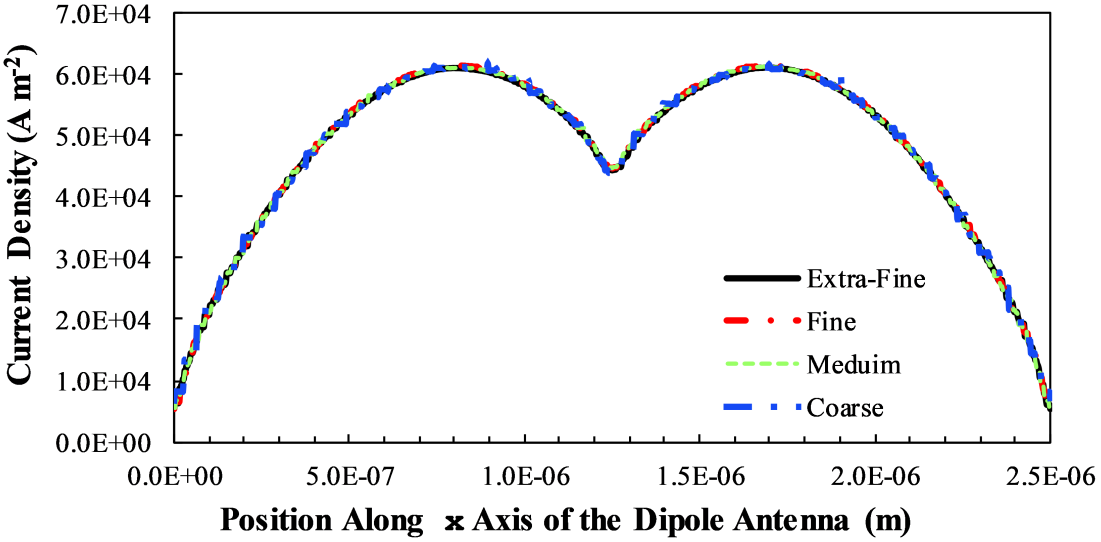

FIGURE 5.15: The distribution of the current along x axis of the dipole antenna for different mesh refinement: coarse, medium, fine and extra-fine.

TABLE 5.7: Impedance extraction obtained by SVS-EFIE for different sizes of the mesh .

Mesh Size	# of Samples per Skin Depth	Impedance
Coarse	1.5 samples	2.045e+02 - 1.603e+02i
Medium	2.0 samples	1.713e+02 - 1.601e+02i
Fine	2.5 samples	1.655e+02 - 1.601e+02i
Extra-Fine	3.0 samples	1.623e-02 - 1.599e+02i

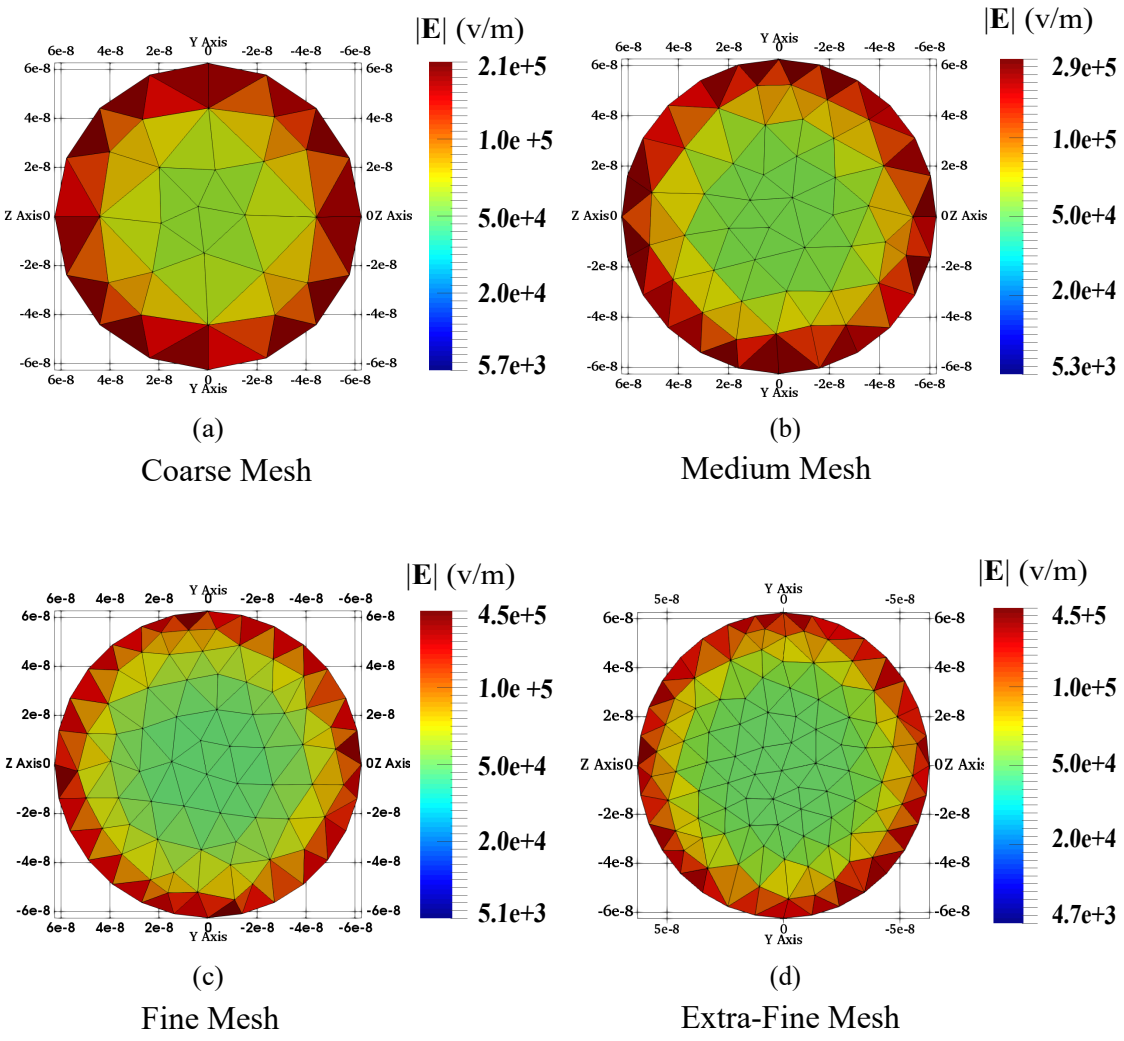

FIGURE 5.16: Current distribution at the surface port of a dipole antenna obtained via MoM solution of SVS-EFIE with different mesh densities: (a) coarse (b) medium (c) fine, and (d) extra-fine corresponding to the 1.5, 2.0, 2.5, and 3.0 samples per skin-depth.

5.4 Analysis of Dipole Antenna with Two Ports Excitation Based on a Surface Integral Equation (EFIE)

The standard surface EFIE solution with δ-gap excitation is known to be unable to provide stable input impedance value of an antenna upon progressive refinement

of the mesh due to charge accumulation at terminals of the port and reactance of the impedance being unable to stabilize [40]. Here, a two-port excitation method is applied in the EFIE solution in order to achieve stable solution when the density of the mesh increases. The δ-gap voltage excitation is applied at one of the ports positioned in the middle of the antenna while the current is measured at the other port which is shifted slightly from its middle. Indeed, the shift of the second port has to be carefully done in such a way that it is sufficiently far from the driven port that current in it is no longer effected by the fringing fields and close enough that the current in it is not too different from its correct value. Systematic choice of the shift between the ports in the two-port model is outside the scope of this thesis. The obtained values of the input impedance in two-port model are shown in Fig. 5.18 and Fig. 5.19. They illustrate stability of the EFIE extracted impedance due to elimination of fringing fields associated with the charge build up at the driven δ-gap port.

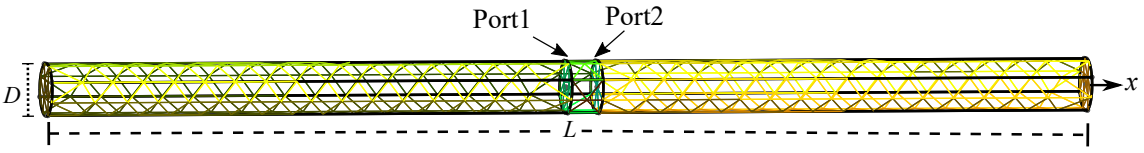

FIGURE 5.17: Dipole antenna with two-port excitation model. Left port is driven with δ-gap voltage while the current is observed at the right port.

The simulation was performed on a dipole antenna made from lead with length $L = 2.5\,\mu\text{m}$ and diameter $D = 62.5\,\text{nm}$, such that the length-to-diameter ratio is $L/D = 40$. Different levels of the mesh were utilized - coarse, medium, and fine. The geometry of the antenna, the material properties, and the operation frequency were fixed for all levels of the mesh density. The characteristic size of the mesh was varied from $1,000$ triangles for the coarse mesh to $20,000$ triangles for the fine mesh. The medium mesh had $10,000$ triangles.

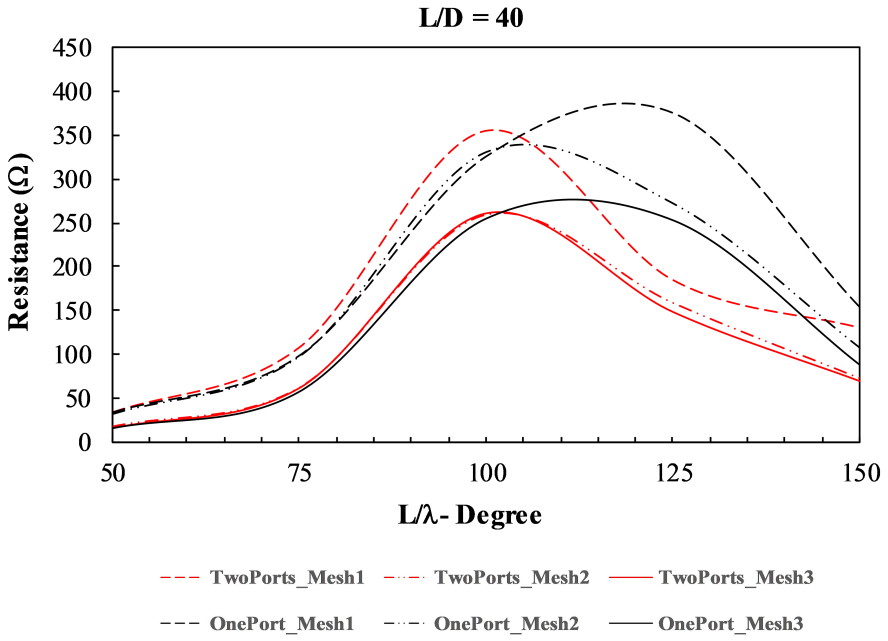

FIGURE 5.18: Input resistance of the dipole antenna obtained by EFIE in one-port and two-ports excitation models.

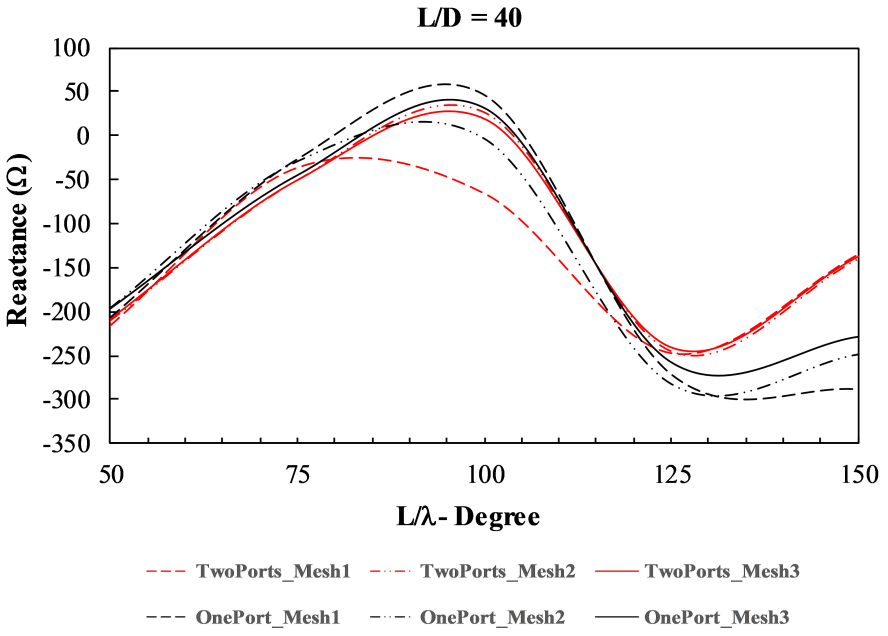

FIGURE 5.19: Input reactance of the dipole antenna obtained by EFIE in one-port and two-port excitation models.

Chapter 6

Conclusions and Future Work

6.1 Conclusions

This works enables application of the Surface-Volume-Surface Electric Field Integral Equation (SVS-EFIE) to solution of the antenna radiation problems and circuit characterization through introduction into it of a port excitation mechanism. Previously SVS-EFIE could be only solved for the cases of incident field excitation such as plane waves, field of a Herzian dipole, and others. The port excitation is introduced into SVS-EFIE through the generalization of the well-known δ-gap model. This generalization includes formation of the right-hand-side in the MoM discretized SVS-EFIE as in the classical surface Electric Field Integral Equation (EFIE) followed by the computation of the net current through the port as the flux of the volumetric polarization current through the cross-section of the port. The new model allows to extract network parameters in complex multi-port circuits and antennas using SVS-EFIE.

The proposed port excitation model is validated through comparisons of the frequency-dependent input impedance computed using SVS-EFIE, obtained experimentally, and computed using classical surface EFIE augmented with Leontovich's surface

impedance operator, the latter being valid under conditions of the strong skin-effect. Good agreement between the impedances extracted using SVS-EFIE and surface EFIE is observed within validity of the loss model in the latter.

Convergence analysis of numerically computed impedance values in the proposed δ-gap driven SVS-EFIE is performed. Stable values of the extracted input impedance are observed in the SVS-EFIE solution upon refinement of the mesh. This shows a clear advantage to the classic surface EFIE solution under δ-gap port excitation which is incapable of reaching stable impedance values upon mesh refinement due to well-known charge accumulation effect producing growing fringing field upon mesh refinement.

6.2 Future Work

- Extend the MoM discretization of the SVS-EFIE to use the hexagonal volume elements and quadrilateral surface elements. Such elements will allow efficient physics based 2-scale MoM discretization of the interconnect structures. The wave physics through the cross-sections of the conductors being governed by the wavelength in metal while the wave physics of propagation along the wires is governed by the wavelength of the external medium (e.g. effective wavelength of the layered medium supporting the conductor). Hence, the cross-sectional size of the mesh elements in MoM discretization should be half the skin-depth, while the longitudinal size of MoM elements should be about 1/10th of the effective wavelength of the surrounding medium. As the latter is thousands of times larger than the former, two-scale MoM discretization of the SVS-EFIE is required for efficient MoM solution of antenna and interconnect analysis problem. In the current implementation of MoM solution of SVS-EFIE used throughout the thesis one-scale discretization based on the skin-depth is used rendering it inefficient.

- Apply the proposed δ-gap model to SVS-EFIE formulation with multi-layered media Green's function.

- Demonstrate the use of δ-gap voltage source model in SVS-EFIE for analysis of complex 3-D interconnects in high-speed links, RF integrated circuits, and other circuits.

- Apply Convergence Acceleration Methods to achieve accurate extracted network parameters (e.g. input impedance in single-port cases) with minimal number of unknowns in the MoM discretization of the SVS-EFIE. The convergence study that has been done in this work has been limited by the capacity of the used H-matrix accelerated MoM solver and machines used.

- Augment classic surface EFIE with the analytic model of the surface impedance for the conductors of circular cross-sections and its solutions of validation of the SVS-EFIE solutions in case of the conductors with circular cross-sections under conditions of both weak and strong skin effects.

Bibliography

[1] M. Al-Qedra, J. Aronsson and V. Okhmatovski, "A novel Skin-Effect Based Surface Impedance Formulation for Broadband Modeling of 3-D Interconnects With Electric Field Integral Equation," *IEEE Trans. Micro. Theory Techn.,* Vol. 58, No. 12, pp. 3871–3881, Dec. 2010.

[2] Y. H. Lo, S. He , L. Jiang and W. C. Chew, "Finite-width gap excitation and impedance models," *IEEE International Symposium on Antennas and Propagation (APSURSI),* Apr. 2011.

[3] K. F. A. Hussein, "Accurate Representation of Excitation and Loading for Arbitrarily Shaped Antennas Composed of Conducting Surfaces in the Method of Moments," *Progress In Electromagnetics Research B,* Vol. 36, pp. 151–171, Jan. 2012.

[4] G. P. Junker, A. A. Kishk and A. W. Glisson, "A novel delta gap source model for center fed cylindrical dipoles," *IEEE Trans. Antennas Propag.,* Vol. 43, No. 5, pp. 537–540, May. 1995.

[5] G. H. Brown and O. M. Woodward, "Experimentally Determined Impedance Characteristics of Cylindrical Antennas," *Proceedings of the IRE*, Vol. 33, No. 4, pp. 257–262, April 1945.

[6] R. Maaskant and M. Arts, "Reconsidering the Voltage-Gap Source Model Used in Moment Methods," *IEEE Trans. Antennas Propag.,* Vol. 52, No. 2, pp. 120–125, Apr. 2010.

[7] J. M. Jin, *The Finite Element Method in Electromagnetics,* 2nd ed. New York: Wiley, 2002.

[8] M. N. O. Sadiku, *Numerical Techniques in Electromagnetics with MATLAB,* CRC Press, 2009.

[9] A. Peterson, S. Ray and R. Mittra, *Computational Methods for Electromagnetics,* New York: IEEE Press, 1998.

[10] E. Bleszynski, M. Bleszynski and T. Jaroszewicz, "Surface integral equations for electro- magnetic scattering from impenetrable and penetrable sheets," *IEEE Antennas Propag. Mag.,* Vol. 35, No. 6, pp. 14–26, Dec. 1993.

[11] C. Müller, *Foundations of the Mathematical Theory of Electromagnetic Waves,* New York: Springer-Verlag, 1969.

[12] A. Kishk and L. Shafai, "Different formulations for numerical solution of single or multibodies of reVolution with mixed boundary conditions," *IEEE Trans. Antennas Propag.,* Vol. 34, No. 5, pp. 666–673, May 1986.

[13] D. Swatek, "Investigation of single-source surface integral equation for electromagnetic wave scattering by dielectric bodies," Ph.D. Thesis, Dept. Electr. Comput. Eng, Univ. Manitoba, Winnipeg, Canada, 1999. [Online]. Available: http://hdl.handle.net/1993/1699.

[14] F. Sheikh Hosseini Lori, A. Menshov, R. Gholami, J. Mojolagbe and V. Okhmatovski, "novel single-source surface integral equation for scattering problems by 3-d dielectric objects," *IEEE Trans. Antennas Propag.*, Vol. 66, No. 2, pp. 797–807, Feb. 2018.

[15] S. Zheng, R. Gholami and V. I. Okhmatovski, "Surface-Volume-Surface Electric Field Integral Equation for Solution of Scattering Problems on 3-D Dielectric Objects in Multilayered Media," *IEEE Trans. Microw. Theory Techn.*, Vol. 66, No. 12, pp. 5399–5414, Dec. 2018.

[16] J. Babatunde Mojolagbe, "Complexity Reduction in Solution of Scattering Problems on Well-Conducting 3-D Object With $\mathcal{H}$ Matrices Accelerated Surface-Volume-Surface Electric Field Integral Equation," M.Sc. Thesis, Dept. Electr. Comput. Eng, Univ. Manitoba, Winnipeg, Canada, 2018. [Online]. Available: http://hdl.handle.net/1993/33088

[17] J. F. Keithley, *The story of electrical and magnetic measurements: From 500 BC to the 1940s*. New York:Wiley-IEEE Press, 1999.

[18] D. K. Cheng, *Field and wave electromagnetics*, New York: Reading, Mass.: Addison-Wesley Pub, 1989.

[19] D. J. Griffiths, *Introduction to electrodynamics*, New York: Prentice Hall, 1998.

[20] W. C. Chew, *Waves and Fields in Inhomogeneous Media,* New York: IEEE Press, 1999.

[21] W. C. Chew, E. Michielssen, J. M. Song and J. M. Jin, *Fast and Efficient Algorithms in Computational Electromagnetics,* norwood, MA, USA: Artech House, 2001.

[22] J. M. Jin, *Theory and Computation of Electromagnetic Fields*, New York: Wiley, 2010.

[23] A. W. Glisson, "An integral equation for electromagnetic scattering from homogeneous dielectric bodies," *IEEE Trans. Antennas Propag.,* Vol. 32, No. 2, pp. 173–175, Feb. 1984.

[24] W. C. Chew, B. Hu and M. S. Tong, *Integral Equation Methods for Electromagnetic and Elastic Waves,* Morgan and Claypool, 2009.

[25] C. T. Tai, *Dyadic Green Functions in Electromagnetic Theory,* 2nd ed. New York: IEEE Press, 1994.

[26] R. Harrington, *Time-Harmonic Electromagnetic Fieldsy,* 1st ed. Wiley-IEEE Press, 2001.

[27] F. Sheikh Hosseini Lori, "Novel single source integral equation for analysis of electromagnetic scattering by penetrable objects," Ph.D. Thesis, Dept. Electr. Comput. Eng, Univ. Manitoba, Winnipeg, Canada, 2017. [Online]. Available: http://hdl.handle.net/1993/32362

[28] J. Kornprobst and T. F. Eibert, "An Accurate Low-Order Discretization Scheme for the Identity Operator in the Magnetic Field and Combined Field Integral Equations," *IEEE Trans. Antennas Propag.*, Vol. 66, No. 11, pp. 6146–6157, nov. 2018.

[29] J. Kornprobst and T. F. Eibert, "A Weak-Form Combined Source Integral Equation With Explicit Inversion of the Combined-Source Condition," *IEEE Antennas Wirel. Propag. Lett.*, Vol. 17, No. 21, pp. 2174–2178, Dec. 2018.

[30] A. Menshov and V. Okhmatovski, "New single-source surface integral equations for scattering on penetrable cylinders and current flow modeling in 2-D conductors," *IEEE Trans. Microw. Theory Techn.*, Vol. 61, No. 1, pp. 341–350, Jan. 2013.

[31] F. Sheikh Hosseini Lori, A. Menshov and V. Okhmatovski, "New vector single-source surface integral equation for scattering problems on dielectric objects in 2-d." *IEEE Trans. Antennas Propag.*, Vol. 65, No. 7, pp. 3794–3799, Jul. 2017.

[32] R. Gholami, A. Menshov and V. Okhmatovski, "$\mathcal{H}$-Matrix Accelerated Solution of Surface-Volume-Surface EFIE for Fast Electromagnetic Analysis on 3-D Composite Dielectric Objects." *IEEE Journal on Multiscale and Multiphysics Computational Techniques*, Vol. 4, No. 7, pp. 152–162, May. 2019.

[33] P. Yla-Oijala M. Taskinen J. Sarvas "Surface integral equation method for general composite metallic and dielectric structures with junctions." *Prog. Electromagn. Res*, Vol. 52, pp. 81–108, 2005.

[34] S. Rao, D. Wilton and A. Glisson, "Electromagnetic scattering by surfaces of arbitrary shape," *IEEE Trans. Antennas Propag.,* Vol. 30, No. 2, pp, 409–418, Jun. 1982.

[35] D. Wilton, S. Rao, A. Glisson, D. Schaubert, O. Al-Bundak and C. Butler, "Potential integrals for uniform and linear source distributions on polygonal and polyhedral domains," *IEEE Trans. Antennas Propag.,* Vol. 32, No. 3, pp. 276–281, Mar. 1984.

[36] N. Kovvali. *Theory and Applications of Gaussian Quadrature Methods*, Morgan and Claypool, 2011.

[37] "EM Fields and Waves," course notes, ETH Zurich Photonics Laboratory, 2014 [Online]. Available https://www.photonics.ethz.ch/fileadmin/userupload/Courses/EMFieldsAndWaves/WaveEquation.pdf

[38] C. A. Balanis, *Antenna theory: Analysis and design*, 3rd ed., Hoboken, NJ: John Wiley, 2005.

[39] D. Cavka and D. Poljak, "Magnetic current loop as a source model for finite thin-wire antennas," *Int. J. Num. Modeling,* Vol. 28, pp. 189–200, 2015.

[40] G. Fikioris and C. Valagiannopoulos, "Input admittances arising from explicit solutions to integral equations for infinite-length dipole antennas," *Progress in Electromagnetics Research,* Vol. 55, pp. 285–306, Jan. 2005.

[41] S. Johnson, J. Whinnery and T. Van Duzer *Field and Waves in Communication Electronics,* 3rd ed. New York: John Wiley & Sons, Inc, 1994.

[42] A. Menshov and V. I. Okhmatovski, "Surface–Volume–Surface Electric Field Integral Equation for Magneto-Quasi-Static Analysis of Complex 3-D Interconnects," *IEEE Trans. Microw. Theory Techn.,* Vol. 62, No. 11, pp. 2563–2573, nov. 2014.

[43] M. S. Yeung, "Single integral equation for electromagnetic scattering by three-dimensional homogeneous dielectric objects," *IEEE Trans. Antennas Propag.,* Vol. 47, No. 10, pp. 1615–1622, Oct. 1999.

[44] R. E. Collin, *Antennas and radiowave propagation,* New York: McGraw-Hill, 1985.

[45] R. C. Johnson, *Antenna Engineering Handbook,* 2nd ed. New York: McGraw-Hill, 1993.

[46] A. Menshov and V. Okhmatovski, "Novel Surface Integral Equation Formulation for Accurate Broadband RL Extraction in Transmission Lines of Arbitrary Cross-Section," *IEEE International Microwave Symposium Digest (MTT),* pp. 1-3, Jun. 2012.

[47] W. Hackbusch, *Hierarchical Matrices Algorithms and Analysis,* Berlin: Springer-Verlag Berlin Heidelberg, 2015.

[48] C. Geuzaine and J. Remacle, "Gmsh: A 3-D finite element mesh generator with built-in pre-and post-processing facilities," *International Journal for Numerical Methods in Engineering*, Vol. 79, No. 11, pp. 1309–1331, 2009, available: http://geuz.org/gmsh/.

[49] A. Squillacote, The ParaView guide: a parallel visualization application. Kitware, 2007, available: http://www.paraview.org/.

[50] MATLAB and Statistics Toolbox Release 2016, The MathWorks, Inc., Natick, Massachusetts, United States.

[51] W. Ding, G. Wang, F. Liang and B. Yuan, "An Enhanced Gap Source Model," *IEEE Trans. Antennas Propag.*, Vol. 61, No. 3, pp. 1266-1272, March 2013.